Materials Chemistry and Physics 312 (2024) 128590

Contents lists available at ScienceDirect

Materials Chemistry and Physics

journal homepage: www.elsevier.com/locate/matchemphys

Full length article

Anisotropic mechanical behavior and thermal attributes of antiferromagnetic UX_2(X=P, As, Sb) materials: A density functional and elasticity theories study

Reyhaneh Ebrahimi-Jaberi, S. Jalali-Asadabadi *

Department of Physics, Faculty of Physics, University of Isfahan (UI), Hezar Jerib Avenue, Isfahan 81746-73441, Iran

HIGHLIGHTS

- Unveiling comprehensive elastic properties of UX_2 (X=P, As, Sb) compounds.
- Decoding the acoustic velocity and its anisotropy in UX_2 materials.
- Charting intricate thermal properties of UX_2, including Debye temperature and heat capacity.
- Highlighting UX_2's suitability for high-temperature applications.

ARTICLE INFO

Keywords:
Mechanical properties
Thermal properties
Wave velocity
Anisotropic behavior

ABSTRACT

In this work, we delve into the investigation of mechanical and thermal properties of antiferromagnetic UX_2 (X=P, As, Sb), which are structured in the unique anti-Cu_2Sb-type tetragonal form. The study's principal findings revolve around the revelation of distinctive compressibility patterns and an observed preference for shear deformation in these compounds. These patterns are notably marked by a lower compressibility along the [100] direction than the [001] one, and the ease of shear deformation on the (100) plane compared to the (001) one. Intriguingly, our findings identify these compounds as residing on the brink of the brittle/ductile borderline as per Pugh's ratio and Poisson's ratio. Furthermore, the mechanical strength in these materials is significantly influenced by shear deformation, a fact indicated by the values of bulk and Young's modulus. Among the UX_2 (X=P, As, Sb) compounds, our analysis of the Debye temperature singles out UP_2 as an outstanding performer due to its higher Debye temperature. A noteworthy aspect of this study is the quicker propagation of longitudinal waves over transverse waves, as indicated by the wave velocity and anisotropy calculations. We bring forth an enriched understanding of the anisotropic behavior of these materials in terms of bulk modulus, Young's modulus, shear modulus, and Poisson's ratio. The predicted high melting temperatures of the UX_2 (X=P, As, Sb) compounds, coupled with the computed heat capacities aligning well with existing experimental data, point towards their potential applicability in high-temperature settings. Collectively, our study not only validates the methodologies employed but also brings to light fascinating new insights into the mechanical and thermal properties of these compounds, deepening our understanding of the intricate interplay between their atomic constitution and physical properties.

1. Introduction

Uranium-based compounds consistently exhibit compelling examples of complex many-body phenomena, such as quantum criticality, heavy fermion superconductivity, and elusive hidden order states [1–10]. Situated at the fascinating intersection of strongly correlated electron systems and itinerant electronic physics, these materials captivate the research community [11]. The intricate balance of physical properties hinges upon the U-U interatomic spacing, the hybridization interplay between 5f electrons and other valence electrons, and specific lattice parameters [12,13]. It is noteworthy that the extent of hybridization between 5f electrons and their valence counterparts is a complex function of several elements, including ligand atom type, and external conditions like pressure and temperature [14].

Amid this complexity, uranium dipnictides UX_2 (X=P, As, Sb) have, over the past two decades, emerged as exemplary representatives of uranium compounds [15–18]. Their appeal resonates both from theoretical [12,14,19–24] and experimental [9,10,15–18,25–34] viewpoints. Their fascination derives from the evolution of properties intimately tied to their electronic structure, which can be elucidated by

* Corresponding author.
E-mail addresses: sjalali@sci.ui.ac.ir, sjalali@phys.ui.ac.ir (S. Jalali-Asadabadi).
URL: https://sciold.ui.ac.ir/~sjalali (S. Jalali-Asadabadi).

https://doi.org/10.1016/j.matchemphys.2023.128590
Received 24 August 2023; Received in revised form 11 October 2023; Accepted 22 October 2023
Available online 27 October 2023
0254-0584/

varying the pnictogen atoms and thereby modulating the hybridization between 5f electrons and conduction electrons [14].

Characterized by the unique anti-Cu_2Sb-type tetragonal structure, these UX_2 (X=P, As, Sb) compounds tantalize researchers with their antiferromagnetic ordering, showcasing remarkable Néel temperatures of 201, 273, and 203 K for UP_2, UAs_2 and USb_2, respectively [21,26,29]. Neutron diffraction findings suggest that their magnetic structure consists of ferromagnetic uranium layers stacked perpendicular to the *c* axis, in an ↑↓↓↑ pattern [27]. As such, the magnetic unit cell of these compounds is twice as large as their chemical unit cell along the elongated *c* axis [15,16,27], further elevating their intriguing properties in the landscape of uranium compounds.

Expanding the scope of inquiry beyond electronic structures and magnetic behaviors, mechanical properties—rooted in a material's molecular architecture—serve as critical determinants of its response to external forces [35]. The significance of these responses escalates when deploying such materials in practical applications, necessitating a nuanced understanding of elasticity [36]. Indeed, the exploration of elasticity and other mechanical properties of a compound is far from a mere academic pursuit—it provides a rich reservoir of insights into the intrinsic behaviors of the material and indications of its practical applicability [37].

Such properties offer a lens through which to scrutinize the material's fundamental characteristics, such as lattice dynamics, phonon spectrum, phase stability, and interatomic potential, as well as thermodynamic functions [37–42]. The present study takes inspiration from the work of Wen et al. [41], who undertook an *ab initio* study of the structural, elastic, and mechanical properties of the B19 TiAl intermetallic compound with an orthorhombic structure. They used density functional theory calculations, specifically the projector augmented wave and the generalized gradient approximation, to optimize structure parameters and confirm mechanical stability. Furthermore, they derived polycrystalline bulk, shear and Young's moduli, Poisson's ratio, Cauchy pressure, and anisotropy factors from single-crystal elastic constants. Their detailed analysis found intrinsic brittleness and elastic anisotropy in B19 TiAl, demonstrating the rich information that can be derived from such computational methodologies, which we have applied to our study of antiferromagnetic UX_2 compounds. Consequently, an exhaustive analysis of UX_2 (X=P, As, Sb) not only illuminates their atomic and magnetic structures but also opens the door to a spectrum of potential technological applications.

Despite the wealth of fascinating research surrounding these materials, the theoretical examination of the elastic properties of antiferromagnetic UX_2 (X=P, As, Sb), especially considering their distinctive anti-Cu_2Sb-type tetragonal structure, is a noteworthy lacuna in our comprehensive understanding. To fill this gap, our study employs the IRelast computational package [43], a product of our own research efforts and the generalized successor of the *cubic-elastic* code [44], which has been implemented within the WIEN2k code [45].

Our research begins with the calculation of the elastic constants for these captivating compounds. Following this foundational step, we forecast and delve into a host of their physical characteristics, encompassing the Kleinman parameter, Pugh's ratio, Poisson's ratio, ductility, and various moduli including bulk, Young's, and shear. We also explore the sound velocities and their anisotropy in these materials, venturing further into the intricate landscape of their physical properties.

Before we delve into the intricacies of our computational investigations, we must first identify the most effective methodologies. In this context, we draw on our prior work [12]. This earlier study explored the electric field gradients (EFGs) at ^{238}U sites for antiferromagnetic UX_2 (X = P, As, Sb, Bi) using LDA, LDA+*U*, PBE-GGA, PBE-GGA+SP+*U*, and the exact exchange for correlated electrons (EECE), among other techniques. The study revealed that most of the band correlated approaches, excluding the EECE method, struggled to reproduce the experimental zero EFG value in UBi_2 accurately. However, it was found that LDA+*U* and PBE-GGA+SP+*U* could successfully calculate nonzero EFGs for other compounds, i.e., UX_2 (X = P, As, Sb), without needing manual adjustments to their initial conditions. The investigation highlighted the influence of magnetic structure, spin arrangement, and the valence electrons in the MT sphere on the EFG. The research also emphasized the role of uranium's magnetic 5f electrons, which contribute to the compound's large effective mass of conduction carriers and influence the EFG of uranium. It was also noted that the density of states (DOS) curves indicated that uranium atoms in UX_2 compounds are magnetic while X atoms are non-magnetic, implying a quasi-two-dimensional property within these compounds.

In light of these findings, we utilized DFT+SP and DFT+SP+SOC in our current study, with LDA [46] and PBE- [47] serving as the exchange–correlation (XC) functionals (XCFs). Here, SP and SOC stand for spin polarization and spin–orbit coupling, respectively. We then assessed these methods' capabilities to reproduce the experimental EFG [18] and the magnetic moment (MM) per uranium atom [21] of the antiferromagnetic phase of UX_2 (X=P, As, Sb).

Recognized as a sensitive measure, the EFG is highly responsive to the asymmetry of both semicore [48] and valence states [49], thus reflecting subtle changes in the electronic DOS [12,50–54]. Our computed EFG and magnetic moments—specifically those procured using PBE-GGA+SP+*U* (U_{eff} = 0.29 Ry), LDA+*U* (U_{eff} = 0.15 Ry), and LDA+*U* (U_{eff} = 0.22 Ry) for antiferromagnetic UP_2, UAs_2, and USb_2 respectively—demonstrate strong concordance with available experimental data [18,21]. Additionally, they are well-aligned with our joint investigations conducted with Ghasemikhah et al. [12]. Therefore, these methods, having been validated, serve as the cornerstone for the elastic calculations in our current work. With this analysis, we aim to scrutinize the degree to which the computational procedures are capable of encapsulating our new elastic findings.

Building on the foundation of our elastic computations and the methodologies validated in collaboration with our previous study [12], we continue to broaden the scope of our investigation. Not satisfied with exploring only the structural properties, we delve deeper into the thermal domain of UX_2 (X=P, As, Sb). We conduct rigorous computations to elucidate a spectrum of thermal properties, including the Debye temperature, melting temperature, thermal expansion, heat capacity, and minimum thermal conductivity. We also scrutinize the anisotropy of these thermal properties, aiming to gain a comprehensive understanding of these intriguing compounds.

In this work, we present an intensive exploration of the mechanical and thermal properties of antiferromagnetic UX_2 (X=P, As, Sb) compounds, featuring the unique anti-Cu_2Sb-type tetragonal structure. We have delved into a broad range of attributes, uncovering distinctive compressibility patterns and a notable preference for shear deformation in these intriguing materials.

We reveal that these compounds lie intriguingly close to the brittle/ductile borderline according to both Pugh's ratio and Poisson's ratio. We also highlight the significant influence of shear deformation on the mechanical strength of these materials, as reflected in the values of bulk and Young's modulus.

From a thermal perspective, our analysis singles out UP_2 due to its elevated Debye temperature. The calculated wave velocities indicate a quicker propagation of longitudinal waves over transverse ones, thereby contributing to our understanding of these materials' anisotropic behavior.

Notably, we calculate and discuss various anisotropic parameters, including the universal anisotropy factor, anisotropy in compression and shear, shear anisotropic factors, and linear compressibility along the *a* and *c* axis. We bring this study to a close by providing a three-dimensional visualization of the bulk modulus, Young's modulus, shear modulus, and Poisson's ratio for these compounds, offering an encompassing perspective of their mechanical properties.

The high melting temperatures we predict for these UX_2 (X=P, As, Sb) compounds, in conjunction with the computed heat capacities that align well with available experimental data, indicate their potential for

Table 1
Experimental lattice parameters in unit of angstroms (Å) for UX_2 (X = P, As, Sb), as reported in scholarly studies by Amoretti et al. [21] and Guziewicz et al. [17], and used in this work.

Compound	a (Å)	b (Å)
UP_2	3.810	7.764
UAs_2	3.954	8.116
USb_2	4.270	8.784

high-temperature applications. This investigation stands as a testament to the precision of our chosen methodologies and illuminates several fascinating aspects of the mechanical and thermal characteristics of these compounds, which could pave the way for future research and potential applications in the field of condensed matter physics.

2. Theory and method

Material science is a domain filled with fascinating and complex phenomena, where the elastic properties of materials play a critical role, forming the basis for a multitude of theoretical insights and practical applications [43]. Elastic constants are paramount in understanding these properties as they represent the response of materials to external forces [39,55–63]. Notably, these constants act as the vital link between the atomic and macroscopic scales, bridging the gap between the micro and macroscopic universes and offering a comprehensive perspective on the material behavior [64–66].

From the foundational elastic constants, we can derive a wealth of physical properties, such as the shear modulus, Reuss's modulus, Voigt's modulus, Young's modulus, Bulk modulus, Hill's modulus, and Poisson's ratio, along with elastic stiffness coefficients and the essential melting temperature [67]. These constants also provide us with the means to calculate sound velocities in various directions and the all-important Debye temperature [68,69]. Utilizing these constants allows us to gain a comprehensive understanding of material behavior.

Elastic constants further extend their utility beyond just mechanical characteristics; they are also key in exploring the thermodynamic properties of materials. For instance, they enable precise determination of the phonon dispersion spectrum, entropy, and thermal expansion coefficient [38,42,70]. They are pivotal in computing the elastic anisotropy ratio, a critical measure in examining the phase stability of crystal structures [71]. In essence, elastic constants serve as a universal tool, illuminating our understanding of fundamental properties and aiding in the optimization of materials for technological applications.

The investigation of elastic constants principally involves two key methodologies—the 'Energy Approach' and the 'Stress Theorem'. Stadler et al. [72] and Wen et al. [73] pioneered the former approach, which hinges on calculating the total ground state energy to determine elastic constants. The emphasis this method places on the energy attributes of materials lends it significant value, providing comprehensive insights into their behavior under varied conditions.

Alternatively, Nielson and Martin [74] proposed the 'Stress Theorem.' This method pivots on the critical interplay between the stress tensor (σ_{ij}) and the strain tensor (ε_{ij}), a correlation that is central to the derivation of elastic constants. The 'Stress Theorem' serves as a mathematically intensive pathway, furnishing in-depth understanding of the material's resilience, deformability, and responses under stress.

In this study, we utilize the 'Energy Approach' methodology as our primary tool in this endeavor to decipher these constants. This approach allows us to effectively calculate elastic constants, specifically tailored for tetragonal compounds. For an in-depth understanding of this innovative approach, we refer interested readers to Ref. [43,44].

In accordance with the principles of Taylor expansion and the paradigm of Hooke's law, the computation of energy for a system subjected to infinitesimal stresses can be described as follows [43]:

$$E(V,\varepsilon_k) = E_0 + V_0\left(\sum_{i=1}^{6}\sigma_i\varepsilon_i + \frac{1}{2}\sum_{i,j=1}^{6}C_{ij}\varepsilon_i\varepsilon_j\right), \tag{1}$$

where ε_k represents the strain components $(\varepsilon_1, \varepsilon_2, \ldots, \varepsilon_n)$. The terms $E(E_0)$ and $V(V_0)$ denote the total energy and volume of the strained (reference) system, respectively. The σ_i are the stress tensor components, while C_{ij} are the components of the elastic stiffness tensor.

As per Eq. (1), the elastic constants (C_{ij}) or their linear terms at zero strain can be calculated by taking the second-order derivative of Eq. (1) as follows [43]:

$$C_{ij} = \frac{1}{V_0}\left(\frac{\partial^2 E}{\partial\varepsilon_i\partial\varepsilon_j}\right). \tag{2}$$

The Bravais lattice vector of a reference system is represented by the R matrix. The lattice distortion, denoted by (R'), can be expressed as $R' = R\times D$. Here, D stands for the deformation matrix, defined as [43]:

$$D = I + \varepsilon = \begin{pmatrix} 1+\varepsilon_1 & \frac{\varepsilon_6}{2} & \frac{\varepsilon_5}{2} \\ \frac{\varepsilon_6}{2} & 1+\varepsilon_2 & \frac{\varepsilon_4}{2} \\ \frac{\varepsilon_5}{2} & \frac{\varepsilon_4}{2} & 1+\varepsilon_3 \end{pmatrix}. \tag{3}$$

Here, I refers to the unit matrix and ε to the symmetric strain tensor. In Eq. (3), we utilized Voigt notation, where xx, yy, zz, zy(yz), zx(xz), xy(yx) are replaced by $1, 2, 3, 4, 5, 6$, respectively [75].

In light of the symmetrical characteristics of tetragonal crystals, we observe six independent components within the matrix of elastic constants. These are represented as C_{11}, C_{12}, C_{13}, C_{33}, C_{44}, and C_{66} [76]. To determine these constants, we must identify six distinct strains. Our methodological tool, the IRelast package, accomplishes this by pinpointing the strains using six distinct distortions, as highlighted in [43,77]:

$$D_1 = \begin{pmatrix} 1+\varepsilon & 0 & 0 \\ 0 & 1+\varepsilon & 0 \\ 0 & 0 & 1 \end{pmatrix}, \tag{4}$$

$$D_2 = \begin{pmatrix} 1+\varepsilon & 0 & 0 \\ 0 & 1+\varepsilon & 0 \\ 0 & 0 & \frac{1}{(1+\varepsilon)^2} \end{pmatrix}, \tag{5}$$

$$D_3 = \begin{pmatrix} 1 & 0 & 0 \\ 0 & 1 & 0 \\ 0 & 0 & 1+\varepsilon \end{pmatrix}. \tag{6}$$

$$D_4 = \begin{pmatrix} \left(\frac{1+\varepsilon}{1-\varepsilon}\right)^{\frac{1}{2}} & 0 & 0 \\ 0 & \left(\frac{1-\varepsilon}{1+\varepsilon}\right)^{\frac{1}{2}} & 0 \\ 0 & 0 & 1 \end{pmatrix}, \tag{7}$$

$$D_5 = \begin{pmatrix} 1 & 0 & \varepsilon \\ 0 & 1 & \varepsilon \\ \varepsilon & \varepsilon & 1+\varepsilon^2 \end{pmatrix}, \tag{8}$$

$$D_6 = \begin{pmatrix} \left(1+\varepsilon^2\right)^{\frac{1}{2}} & \varepsilon & 0 \\ \varepsilon & \left(1+\varepsilon^2\right)^{\frac{1}{2}} & 0 \\ 0 & 0 & 1 \end{pmatrix}. \tag{9}$$

By utilizing Eq. (1), we are equipped to compute the total energy of the system when exposed to the aforementioned strains [43]. This computation is accomplished through the following set of equations, each corresponding to a specific strain:

$$E_{D_1}(V,\varepsilon) = E_0 + V_0\left\{(C_{11}+C_{12})\,\varepsilon^2 + O\,(\varepsilon^3)\right\}, \tag{10}$$

$$E_{D_2}(V,\varepsilon) = E_0 + V_0\left\{(C_{11}+C_{12}+2\,C_{33}-4\,C_{13})\,\varepsilon^2 + O\,(\varepsilon^3)\right\}, \tag{11}$$

$$E_{D_3}(V,\varepsilon) = E_0 + V_0\left\{\frac{C_{33}}{2}\,\varepsilon^2 + O\,(\varepsilon^3)\right\}, \tag{12}$$

$$E_{D_4}(V,\varepsilon) = E_0 + V_0\left\{(C_{11}-C_{12})\,\varepsilon^2 + O\,(\varepsilon^4)\right\}, \tag{13}$$

$$E_{D_5}(V,\varepsilon) = E_0 + V_0\left\{4\,C_{44}\,\varepsilon^2 + O\,(\varepsilon^4)\right\}, \tag{14}$$

Table 2
Electric field gradient (EFG) values per uranium atom in antiferromagnetic UX_2 (X=P, As, Sb) compounds: The compounds are crystallized in their anti-Cu_2Sb-type tetragonal structure and EFG units are presented as 10^4 V nm^{-2}. Calculations were performed using both LDA+SP+U(+SOC) and PBE-GGA+SP+U(+SOC) methods, with an effective Hubbard parameter U_{eff} between 0.15 and 0.29 Ry. Here, SP indicates spin-polarization, SOC denotes spin–orbit coupling, and U_{eff} refers to the effective Hubbard parameter. Data calculated with SOC is in parentheses, and our study's results are marked with *. Blank cells indicate repetition from the cell above.

Scheme	SP	SOC	U_{eff} (Ry)	UP_2	UAs_2	USb_2	Ref.
LDA	Yes	No (Yes)		1.51 (1.45)	1.38 (1.34)	1.17 (1.14)	*
LDA+U			0.15	1.39 (1.24)	1.39 (1.40)	1.24 (1.04)	*
			0.22	1.43 (1.37)	1.59 (1.34)	1.21 (0.98)	*
			0.29	1.61 (1.47)	1.58 (1.37)	1.14 (0.91)	*
PBE-GGA				1.38 (1.33)	1.34 (1.29)	1.17 (1.12)	*
PBE-GGA+U			0.15	1.35 (1.22)	1.49 (1.52)	1.23 (1.08)	*
			0.22	1.51 (1.35)	1.59 (1.41)	1.17 (1.03)	*
			0.29	1.61 (1.42)	1.67 (1.50)	1.21 (0.94)	*
LDA				1.544 (1.501)	1.409 (1.412)	1.237 (1.287)	[12]
LDA+U		Yes	0.13	1.260	1.306	1.182	[12]
PBE-GGA		No (Yes)		1.423 (1.391)	1.353 (1.365)	1.227 (1.275)	[12]
PBE-GGA+U		Yes	0.13	1.244	1.303	1.195	[12]
LDAFock				1.269	1.346	1.277	[12]
B3PW91				1.202	1.377	1.293	[12]
WCFock				1.246	1.311	1.261	[12]
PBEsol				1.262	1.317	1.280	[12]
PBEFock				1.215	1.295	1.283	[12]
Exp.				2.1 ± 0.5	1.5 ± 0.3	1.6 ± 0.4	[18]

$$E_{D_6}(V,\varepsilon) = E_0 + V_0\left\{2\ C_{66}\ \varepsilon^2 + O\ (\varepsilon^4)\right\}, \tag{15}$$

where energy $E_{D_i}(V,\varepsilon)$ corresponds to the given distortion D_i, for $i = 1$ to 6. Note that each equation represents a different stress–strain condition and includes the strain term to the second power or higher (represented by the $O\ (\varepsilon^3)$ and $O\ (\varepsilon^4)$ terms), signifying the non-linear relationship between stress and strain.

Building upon the total energy equations detailed earlier, we can proceed to obtain the elastic constants of a tetragonal crystal by applying the second derivative. This mathematical operation enables us to examine the rate of change of the system's total energy, revealing the system's response to variations in strain:

$$\frac{\partial^2 E_{D_1}}{\partial \varepsilon^2} = 2V_0(C_{11} + C_{12}), \tag{16}$$

$$\frac{\partial^2 E_{D_2}}{\partial \varepsilon^2} = 2V_0(C_{11} + C_{12} + 2\ C_{33} - 4\ C_{13}), \tag{17}$$

$$\frac{\partial^2 E_{D_3}}{\partial \varepsilon^2} = V_0 C_{33}, \tag{18}$$

$$\frac{\partial^2 E_{D_4}}{\partial \varepsilon^2} = 2V_0(C_{11} - C_{12}), \tag{19}$$

$$\frac{\partial^2 E_{D_5}}{\partial \varepsilon^2} = 8V_0 C_{44}, \tag{20}$$

$$\frac{\partial^2 E_{D_6}}{\partial \varepsilon^2} = 4V_0 C_{66}. \tag{21}$$

As seen from these equations, each second derivative of the total energy in respect to strain corresponds to a particular combination of elastic constants, multiplied by the equilibrium volume, V_0.

3. Details of calculation

Having established the theoretical framework for investigating elastic properties in tetragonal crystals, we now turn our attention to the empirical aspect of this study. Our particular interest lies in the antiferromagnetic compounds UX_2 (X=P, As, Sb), notable for their distinctive anti-Cu_2Sb-type tetragonal structure. This unique structure, as we illustrated in Fig. 3(b) of Ref. [12], is expected to yield intriguing insights into the elastic behaviors of these compounds.

Here, we effectively utilize the robust computational capabilities of the IRelast package, named after Iran (IR), to probe the elastic constants of antiferromagnetic UX_2 (X=P, As, Sb) compounds within their anti-Cu_2Sb-type tetragonal structures. Implemented within the WIEN2k code framework [45], the IRelast tool capitalizes on density functional theory (DFT) [78,79] to solve the Kohn–Sham equations [79] via the full-potential augmented planewaves plus local orbitals (FP-APW+lo) method [80,81]. In the quest to decipher the elastic constants, we harness the 'Energy Approach' methodology, a unique strategy designed by IRelast particularly for tetragonal compounds. For a comprehensive understanding of this advanced computational package and its methodological foundations, we direct interested readers to Ref. [43,44].

In order to delve into the spatial variations of linear compressibility (β), Young's modulus (E), shear modulus (G), and Poisson's ratio (ν) within the (xy), (xz), and (yz) planes of the crystal structure, we utilized the ELATE code [82]. This tool, established by Romain Gaillac, Pluton Pullumbi, and François-Xavier Coudert, is an open-source application that permits the thorough analysis and visualization of elastic tensors, which in our case, were computed using the IRelast package. Through its graphical representations and detailed computational capabilities, ELATE serves as an invaluable asset in examining the anisotropies and complexities of mechanical properties within these antiferromagnetic UX_2 compounds.

In our study, we rely on experimental data to ensure our calculations align with observed natural phenomena. Specifically, we integrate the experimentally determined lattice parameters (Table 1), obtained through X-ray diffraction techniques [17,21], into our calculations.

For our calculations, we adopt a $11 \times 11 \times 2$ k-point mesh following the Monkhorst–Pack scheme [83]. Other chosen parameters include $l_{max} = 10$ and $k_{max} = 7/R_{MT}$, where l_{max} is the maximum value of l within the atomic sphere, k_{max} is the plane wave cut-off, and R_{MT} is the radii of all atomic spheres [84]. We also utilize a value of $G_{max} = 14$ (Bohr)$^{-1}$ for the Fourier expansion of the charge density.

3.1. Electric field gradients, and magnetic moments

In our quest to determine the most suitable exchange–correlation functional for the evaluation of elastic properties, we calculate both the electric field gradient and the total magnetic moment per uranium atom for the compounds UX_2 (X=P, As, Sb). To achieve this, we utilize the local density approximation (LDA) [46] and the Perdew–Burke–Ernzerhof generalized gradient approximation (PBE-GGA) [47].

While we acknowledge that these approximations might be inadequate for strongly correlated materials like our target compounds [85],

Table 3
Magnetic moment per uranium atom for UX_2 (X=P, As, Sb) compounds: Displayed in units of μB, the total magnetic moments are computed using LDA+SP+U(+SOC) and PBE-GGA+SP+U(+SOC) methods within the effective Hubbard parameter (U_{eff}) range of 0.15 to 0.29 Ry. Here, SP represents spin-polarization, SOC refers to spin–orbit coupling, and results obtained in our study are marked with *. Values in parentheses include SOC. Empty cells represent repeated values from the cell above.

Scheme	SP	SOC	U_{eff} (Ry)	UP_2	UAs_2	USb_2	Ref.
LDA	Yes	No (Yes)		0.92 (0.72)	1.33 (1.09)	1.59 (1.33)	*
LDA+U			0.15	1.35 (1.25)	1.61 (1.44)	1.80 (1.72)	*
			0.22	1.55 (1.44)	1.77 (1.73)	1.83 (1.78)	*
			0.29	1.72 (1.55)	1.75 (1.74)	1.83 (1.78)	*
PBE-GGA				1.09 (0.91)	1.42 (1.23)	1.65 (1.44)	*
PBE-GGA+U			0.15	1.48 (1.12)	1.73 (1.08)	1.80 (1.16)	*
			0.22	1.68 (1.16)	1.81 (1.15)	1.84 (1.07)	*
			0.29	1.76 (1.13)	1.80 (0.95)	1.98 (1.07)	*
WCFock		Yes		1.274	1.645	2.223	[12]
PBE-GGA					0.9 ± 0.01	0.7 ± 0.1	[14]
Exp.				2.0 ± 0.1	1.61 ± 0.11	1.88 ± 0.03	[21]

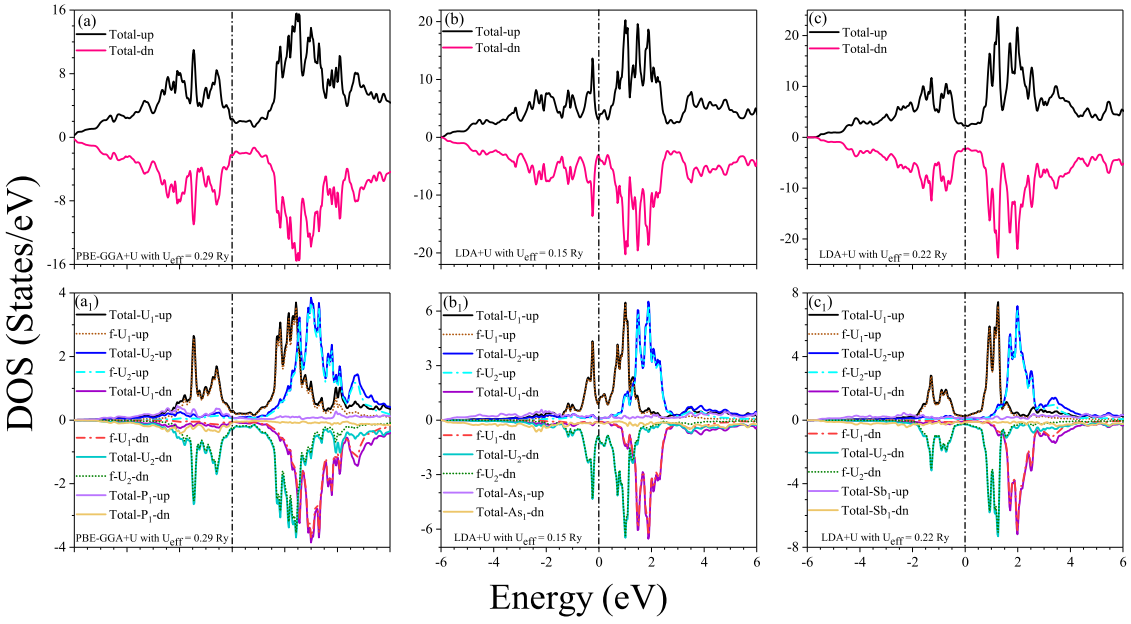

Fig. 1. Density of states (DOS) for Antiferromagnetic UP_2, UAs_2, and USb_2: Total and projected DOSs calculated using PBE-GGA+SP+U (U_{eff} = 0.29 Ry), LDA+SP+U (BXMATH[110], and LDA+SP+U (U_{eff} = 0.22 Ry) are shown for compounds in their anti-Cu_2Sb-type tetragonal structure, where SP and U_{eff} represent the spin-polarization and effective Hubbard parameter, respectively.

we augment them with the Hubbard parameter [86–89] which is known to handle such complex materials effectively. In this scenario, we evaluate various values of the effective Hubbard parameter, U_{eff}, defined as $(U - J)$.

The outcomes of our calculations for the electric field gradient and the total magnetic moment per uranium atom are compiled in Tables 2 and 3, respectively. Considering the strong relativistic effects induced by the 5f electrons in UX_2 (X=P, As, Sb), we undertake our calculations in two distinct conditions—both with and without spin–orbit coupling (SOC).

In our pursuit of accuracy within the latest versions of the codes used, we compare our results to available experimental data and previous theoretical works. This comparison reveals that using PBE-GGA+SP+U (U_{eff} = 0.29 Ry) for UP_2, LDA+U (U_{eff} = 0.15 Ry) for UAs_2, and LDA+U (U_{eff} = 0.22 Ry) for USb_2, provide the closest alignment with the reference data, considering both the electric field gradient and total magnetic moment per uranium atom. Therefore, these approximations underpin our calculations of the elastic properties.

For an in-depth exploration of electric field gradients and magnetization, we recommend referring to Ref. [12], which offers a comprehensive discussion on the subject. In our study, our primary objective has been to validate the precision of the updated versions of the codes in question by replicating the experimental results for sensitive parameters, such as the electric field gradient and magnetization. This rigorous validation helps boost our confidence in the accuracy of our elastic results, especially considering the lack of experimental data for these results.

3.2. Densities of states

Here, we focus on validating the accuracy of the updated computational codes, specifically in terms of their capacity to replicate DOSs faithfully. To this end, we investigate the total and projected density of states (DOS) for UP_2 (Figs. 1(a) and (a_1)), UAs_2 (Figs. 1(b) and (b_1)), and USb_2 (Figs. 1(c) and (c_1)) within their anti-Cu_2Sb-type tetragonal structure. We utilize PBE-GGA+SP+U (U_{eff} = 0.29 Ry), LDA+SP+U (U_{eff} = 0.15 Ry), and LDA+SP+U (U_{eff} = 0.22 Ry) for UP_2, UAs_2, and USb_2 respectively. The figures reveal nonzero total DOS at the Fermi energy, suggesting that UX_2 (X=P, As, Sb) are conductors. The dash-dot line set to the zero point represents the Fermi energy. Furthermore, the symmetry of the up and down states of total DOS graphs, see Figs. 1(a), (b), and (c), indicates the antiferromagnetic phase in UX_2 (X=P, As, Sb).

In Figs. 1(a_1), (b_1), and (c_1), the unequal densities of up and down states for U(1) and U(2) validate the presence of local magnetic moments in uranium atoms. Interestingly, the up DOS for U(1) equals

the down DOS for U(2), and vice versa. This balance suggests that the magnetic moments of U(1) and U(2) are equal in magnitude but opposite in direction, thereby canceling each other out. Consequently, the net magnetic moment of the compounds is zero. This aligns with experimental findings [21,26,29], confirming the antiferromagnetic phase of UX_2 (X=P, As, Sb). Thus, although uranium atoms possess local magnetic moments, they do not contribute to the total magnetic moment of the compounds under study.

DOSs for atoms X=P, As, Sb within UX_2 are displayed in Figs. 1(a_1), (b_1), and (c_1). These figures illustrate the symmetric up and down states of X atoms, signifying their non-magnetic nature in the studied compounds. The nonzero DOSs near the Fermi energy for both U and X atoms indicate their joint contribution to the conduction process. Notably, U atoms contribute dominantly to the DOSs near the Fermi energy, underscoring their crucial role in conduction—specifically the f orbitals within these U atoms, as evidenced in Figs. 1(a_1), (b_1), and (c_1).

For a comprehensive analysis of densities of states (DOSs), we recommend readers refer to Ref. [12], which discusses the topic extensively. The research illustrates that the partial DOSs for the f orbital of uranium in UBi_2 and USb_2 compounds are very similar, exhibiting differences mainly in the peaks' heights. Furthermore, it has been shown that the contributions from the down spin states below the Fermi energy are negligible, as most of the DOS curves within this energy interval correspond to up spin states.

The DOS curves also reveal that the uranium atoms in all UX_2 compounds exhibit magnetic properties, while the X atoms are non-magnetic. This results in a unique configuration where magnetic planes of uranium are interspersed with non-magnetic X planes, thus imparting a quasi-two-dimensional character to these compounds. Interestingly, the f orbital DOS curve exhibits a nonzero value on the Fermi surface, indicating the involvement of f orbital electrons in the conduction process. These electrons exhibit varying degrees of localization across different compounds. The significant role of uranium's 5f electrons in contributing to UX_2's effective mass of conduction carriers and the conduction process in these compounds is another key takeaway. The 5f orbital, being the magnetic orbital of uranium, has a profound impact on the atom's magnetization, significantly affecting the electric field gradient (EFG) of uranium. Our calculated magnetic moments for uranium in different compounds also align well with experimental results, marking an improvement over previous calculations, which had significantly underestimated these values.

The above thorough validation process is essential to support the credibility of our elastic results, particularly in the absence of corresponding experimental data. To verify the effectiveness of this effort, we looked to the findings presented in Ref. [12]. This source provided a detailed exploration of the DOSs of the f orbital (where $l = 3$), accounting for all seven possible values of the m quantum number. For a more visual understanding of these distributions, we direct readers to Fig. 7 of Ref. [12]. The findings and their agreement with the results presented in Ref. [12] validate the accuracy of the employed approximations. By ensuring the codes' ability to accurately reproduce these DOSs, we can confidently assert the reliability of our study's elastic results.

3.3. Dynamical stability

In our subsequent sections, we will pivot our focus towards exploring the mechanical stability of the systems under study by delving into the elastic constants. It is also imperative to extrapolate our findings to deduce structural stability, which underpins material performance at a fundamental level. Henceforth, we will elucidate the dynamical stability of the UX_2 (X=P, As, Sb) compounds, harnessing the frozen phonon approach facilitated by the Phonopy package [90].

To achieve this, we constructed a $(2 \times 2 \times 1)$ supercell, containing $24(= 6 \times 2 \times 2 \times 1)$ atoms, derived from the original tetragonal structure, which inherently houses 6 atoms with 5 non-equivalent atoms. Grounded in the lattice dynamics theory [91,92], we meticulously evaluated the atomic forces in our candidate materials. This necessitated atomic displacement, post which the resultant forces on each atom were ascertained via DFT methodologies [78,79], abiding by the Hellman–Feynman theorem [93–96].

Consequently, the elements of the dynamical matrix, $D^{kk'}_{\mu\nu}(\boldsymbol{q}_j)$, were calculated for each material, with indexes μ and ν representing Cartesian force directions, and k and k' enumerating atomic units. Through the frozen-phonon paradigm, we discerned the normal modes, $\omega(\boldsymbol{q}_j)$, for every wavevector $\boldsymbol{q}_j$. By solving for eigenvalues, $\omega^2(\boldsymbol{q}_j)$, of these matrices, the phonon spectra for our crystals were delineated.

It is essential to note the Hermitian nature of the dynamical matrix ensures its eigenvalues remain real. However, pure imaginary eigenvalues, though mathematically feasible, are physically incongruous since they imply unbounded phonon wave amplitude. Systems exhibiting these are classified as 'dynamically unstable.' By convention, such systems have negative frequencies, marking them distinct from the positive ones that correspond to real eigenvalues. Thus, the graphical representations of our phonon dispersions for UX_2 (X=P, As, Sb) are outlined in Fig. 2, showcasing these dynamics along the 1BZ's symmetrical pathways.

Dynamical stability remains a core tenet for understanding material behavior, serving as a direct indicator of the system's propensity to maintain or return to its equilibrium state upon atomic displacements. In essence, it implies that the system's potential energy consistently rises, regardless of the specific atomic displacements within the compound [97]. Phononic behavior offers a nuanced lens into this aspect. If a system is truly dynamically stable, its phonons, which represent quantum of vibrational energy in the lattice, should not exhibit negative frequencies.

But what underpins this assertion? Simply put, the positive frequency of phonons denotes an increase in potential energy when atoms are displaced from their equilibrium positions, subsequently leading to restoration forces aiming to revert the system to its equilibrium [97]. Conversely, negative frequencies are emblematic of a decrease in potential energy for certain atomic displacements, signifying the system's innate predisposition to further deviate from equilibrium, rather than restore it [97]. Such behavior is unequivocally indicative of dynamical instability.

Our phonon dispersion results for UX_2 (X=P, As, Sb) are meticulously cataloged in Fig. 2. A discerning analysis reveals a significant observation: all phononic branches squarely reside within positive frequencies for each compound under scrutiny. Thus, mirroring the theoretical premise, our findings robustly attest to the absence of negative phononic frequencies. The implications are profound: the UX_2 (X=P, As, Sb) compounds exhibit dynamical stability. This validation not only underscores the robustness of our chosen structures but also lends weight to their relevance and applicability in subsequent research endeavors.

4. Results and discussions

In the following section and its associated subsections, we endeavor to undertake a pioneering discussion of the elastic properties for UX_2 (where X represents P, As, or Sb). We hope that this first-time analysis will provide valuable insights and stimulate further research in this area.

4.1. Elastic properties

As we delve deeper into the physical properties of antiferromagnetic UX_2 (X=P, As, Sb) compounds, the discussion naturally gravitates towards their elastic characteristics, pivotal for a broad spectrum of practical applications as well as for advancing theoretical understanding. Utilizing the method outlined in Section 3 and validated in Sections 3.1

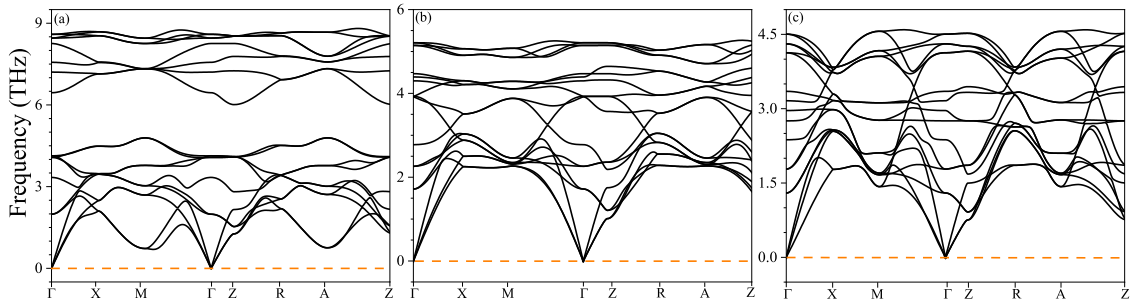

Fig. 2. Phonon dispersion curves for (a) UP_2, (b) UAs_2, and (c) USb_2. The horizontal dashed line indicates the zero frequency.

Table 4
Elastic constants of antiferromagnetic UP_2, UAs_2, and USb_2: We present our calculated elastic constants (C_{ij}) for these compounds in their anti-Cu_2Sb-type tetragonal structure, using PBE-GGA+SP+U (U_{eff} = 0.29 Ry), LDA+SP+U (U_{eff} = 0.15 Ry), and LDA+SP+U (U_{eff} = 0.22 Ry). SP and U_{eff} denote spin-polarization and the effective Hubbard parameter, respectively. Our results are marked by *. To avoid redundancy in the table, any blank cell under the 'Compound' or 'Code' columns takes on the value of the cell immediately above it.

Compound	XCFs	U_{eff} (Ry)	C_{11} (GPa)	C_{12} (GPa)	C_{13} (GPa)	C_{33} (GPa)	C_{44} (GPa)	C_{66} (GPa)	Code	Ref.
UP_2	PBE-GGA+SP+U	0.29	225.602	125.366	99.827	293.908	78.680	114.507	WIEN2k	*
UAs_2	LDA+SP+U	0.15	161.081	99.189	39.380	148.192	59.434	79.970		*
USb_2	LDA+SP+U	0.22	134.796	89.252	38.023	127.330	43.561	78.705		*
USi_2	PW91-GGA		189.8	106.5	71.3	179.0	77.7	106.5	CASTEP	[98]
	PBEsol-GGA+U	0.147	193	124	95	250	75	135		[99]
	PBE-GGA+SP		187.2	88.9	58.6	190.7	70.3	124.8	VASP	[100]
	PBE-GGA		197.7	128.0	90.3	238.6	82.2	130.5		[100]
ThS_2	PBE-GGA		203.0	65.8	54.2	188.7	81.1	60.0		[101]

and 3.2, we can compute their elastic constants, which are summarized in Table 4.

In this table, we primarily focus on two elastic constants: C_{11} and C_{33}. They respectively correspond to the resistance of the material to linear compression along the crystallographic [100] and [001] directions [102]. A nuanced understanding of these constants is instrumental in unveiling the fundamental aspects of their crystal structure and bonding properties. Our work shares some parallels with the comprehensive investigation of topological Weyl semimetals TaX (X = P, As) conducted by Naher and Naqib [102]. Their work, based on the first-principles method using density functional theory, extensively studied a host of properties including structural, elastic, mechanical, electronic, bonding, acoustic, thermal, and optical attributes of these semimetals. They reported a blend of ionic and covalent bonding characteristics, relatively high Vickers hardness, low Debye and melting temperatures, and semi-metallic features with quasi-linear energy dispersions, among other findings. They also found these compounds to be efficient absorbers of ultraviolet radiation and possess high reflectivity across a wide spectral range, contributing to their potential use as reflective coatings. Their findings and methodologies serve as an important reference in our investigation of antiferromagnetic UX_2 compounds.

Our analysis reveals an intriguing pattern: across all UX_2 (X=P, As, Sb) compounds, C_{11} consistently surpasses C_{33}. This indicates a heightened resistance to linear compressibility along the [100] direction in comparison to the [001] direction. It is a testament to the anisotropic nature of these materials, which could have far-reaching implications for their mechanical resilience and applications in various stress conditions.

A closer scrutiny of the constants across different compounds provides further insights. USb_2 emerges as the compound with the greatest compressibility, closely followed by UAs_2 and UP_2. This hierarchy suggests a systematic variation in the elastic properties as a function of the X species in UX_2, pointing towards a potential role of the chemistry of these materials in influencing their mechanical behavior.

Altogether, these findings not only unravel the elastic nature of these uranium-based compounds but also expose their intricate anisotropic behavior. This opens up an exciting avenue of exploration to understand how such unique physical traits could be harnessed for engineering materials with tailored properties.

Continuing our exploration of the elastic properties of antiferromagnetic UX_2 (X=P, As, Sb) compounds, we now turn our attention to the elastic constant C_{44}. This constant signifies the resistance of these compounds to shear deformation when tangential stress is applied along the [010] direction on the (100) plane [102]. The shear deformation reflects the material's ability to withstand shape changes without any volume alteration, thereby giving us insight into its ductility and mechanical stability.

An interesting revelation emerges from the data—for all the compounds investigated, C_{44} is found to be lower than both C_{11} and C_{33}. This tells us that these compounds are more inclined to deform through shear processes rather than by linear compressibility along any of the main crystallographic directions. This propensity to favor shear deformation potentially uncovers a new aspect of these compounds' mechanical behavior, and could have profound implications for their response under specific mechanical or stress conditions.

To add further depth to our understanding, we also examine C_{66}, another critical elastic constant. Remarkably, the values for C_{66} consistently outstrip those of C_{44}. This observation indicates that, among the different planes in the crystal structure of UX_2 compounds, the (100) plane is more easily deformed by shear stress than the (001) plane.

Our study introduces a unique dimension to the current landscape of material research, especially when observing the UX_2 (X=P, As, Sb) compounds. As of now, both theoretical and experimental studies are conspicuously absent in literature regarding these compounds within the space group P4/nmm. This void not only poses challenges in terms of direct comparative analyses but also paves the way for groundbreaking research opportunities and findings. To ensure the credibility and validity of our results in this pioneering endeavor, we adopted a systematic strategy. Recognizing the importance of context, we sought analogues or parallels in the realm of established compounds that could mirror the structural or space group characteristics of our subjects of interest. Our exploration led us to the tetragonal USi_2 [98–100] and ThS_2 [101] compounds. Intriguingly, these compounds manifest structural attributes that resonate strongly with the ones we are investigating, offering a valuable benchmark for comparison. Table 4 offers a detailed comparative insight into the elastic constants of our researched compounds vis-à-vis those of USi_2 and ThS_2. The close congruence between our computed elastic constants and those of these

Table 5
Kleinman Parameter, bulk modulus, shear modulus, Young's modulus, Pugh's Ratio, Vicker's hardness, and Poisson's Ratio for UP_2, UAs_2, and USb_2: This table presents calculated values of the Kleinman parameter (ζ), bulk modulus (B) (GPa), shear modulus (G) (GPa), Young's modulus (E) (GPa), Pugh's ratio (G/B), Vicker's hardness H_V (GPa), and Poisson's ratio (ν) for these antiferromagnetic compounds in the anti-Cu_2Sb-type tetragonal structure. Calculations were made using PBE-GGA+SP+U (U_{eff} = 0.29 Ry), LDA+SP+U (U_{eff} = 0.15 Ry), and LDA+SP+U (U_{eff} = 0.22 Ry), with SP and U_{eff} denoting spin-polarization and the effective Hubbard parameter, respectively.

Compound	XCFs	ζ	B (GPa)	G (GPa)	E (GPa)	G/B	H_V (GPa)	ν
UP_2	PBE-GGA+SP+U	0.671	154.640	79.485	203.575	0.514	8.872	0.280
UAs_2	LDA+SP+U	0.720	90.334	56.225	139.692	0.622	9.129	0.242
USb_2	LDA+SP+U	0.756	79.663	44.887	113.368	0.563	6.463	0.262

reference compounds not only vouches for the accuracy and reliability of our research methodology but also underscores the shared mechanical nuances inherent in these materials. But our findings transcend mere numerical comparisons. They forge a deeper understanding of the mechanical intricacies of these compounds, potentially leading to practical applications. The correlation established with USi_2 and ThS_2 does not just serve as an endorsement of our research accuracy; it further elucidates the potential mechanical behaviors and broader applications of the UX_2 compounds, bridging the often expansive chasm between theoretical forecasts and tangible, real-world utility.

Collectively, these results contribute to our understanding of the deformation mechanisms operative in these uranium compounds. This knowledge could prove invaluable in tailoring these materials for specific applications where resistance to certain types of stress and deformations is paramount. Moreover, the clear distinction between the various types of deformation resistance provides a rich context for future theoretical and experimental studies, paving the way for new insights into the physics of these complex materials.

Building on our previous discussions regarding the elastic constants of UX_2 (X=P, As, Sb) compounds, we now focus on the implications of the relationship between $C_{11} + C_{12}$ and C_{33}. Interestingly, it is observed that $C_{11}+C_{12}$ consistently surpasses C_{33} across all compounds. This suggests a contrast in the elasticity between different orientations within the crystal structure: while the bonding within the (001) plane displays higher rigidity, the bonding along the c axis exhibits greater elasticity. This difference could have significant effects on the compound's mechanical response under various stress conditions, and could potentially unveil distinct aspects of its physical behavior.

Furthermore, as we shift our attention to the elastic constants' trends across different compounds, we observe a systematic decrease in their values moving from P to As, and then from As to Sb in UX_2 compounds. This trend could be intimately linked to an increase in the lattice parameter across these compounds. As the lattice parameter represents the physical dimensions of the unit cell, its increase may reflect an expansion of the crystal structure, which, in turn, may lessen the atomic forces responsible for elastic resistance, hence leading to lower elastic constants.

This connection between the lattice parameter and elastic constants might provide a novel perspective for understanding the underlying physics that govern the mechanical properties of these uranium compounds. It also underscores the importance of comprehending the structure–property relationship in these materials, which may be instrumental in fine-tuning their properties for targeted applications. Furthermore, this trend, once thoroughly understood, could serve as a guiding principle for predicting the mechanical behaviors of similar compounds, thus expanding our knowledge base of the physics underlying these fascinating materials.

Elastic constants represent a powerful tool for not only assessing the resistive behavior of materials to deformation but also probing their inherent stability. Specifically for tetragonal crystals, such as the antiferromagnetic UX_2 (X=P, As, Sb) compounds we are studying, the Born stability criteria play a pivotal role [103–105]. These criteria constitute a set of vital conditions the elastic constants must fulfill to ensure the material's mechanical stability. In detail, they are presented as:

$$C_{11} > 0,\ C_{33} > 0,\ C_{44} > 0,\ C_{66} > 0, \tag{22}$$

$$C_{11} - C_{12} > 0,\ C_{11} + C_{33} - 2\ C_{13} > 0, \tag{23}$$

$$2\ C_{11} + C_{33} + 2\ C_{12} + 4\ C_{13} > 0. \tag{24}$$

Satisfying these conditions implies that the crystal structure is mechanically stable, resistant to spontaneous transformation, and is robust against small distortions. This intrinsic stability links back to the fundamental physics of the material, possibly indicating a well-defined and stable energy landscape. On the contrary, failure to meet these criteria might suggest a predisposition towards structural phase transitions under specific conditions. This potential instability can introduce new possibilities for understanding and manipulating the properties of these compounds, thus providing potential avenues for novel applications. Analyzing our UX_2 (X=P, As, Sb) compounds under the lens of these criteria allows us to explore their mechanical stability and consequently, the underlying physics that governs their behavior. This, in turn, may offer fascinating insights into their macroscopic behavior and open up potential applications that leverage these unique properties. Thus, we will scrutinize these Born criteria and probe what new physics they might unveil about our compounds under consideration.

Our investigation into the mechanical stability of the UX_2 (X=P, As, Sb) compounds, leveraging the calculated elastic constants as detailed in Table 4, indicates that they fulfill the Born stability conditions. This confirmation endorses the structural robustness of these compounds, a critical characteristic for both fundamental research and applications. Moving forward, we delve deeper into their stability characteristics, specifically focusing on the resistance against bending and stretching. To this end, we introduce a dimensionless parameter known as Kleinman's internal displacement parameter (ζ). This valuable measure serves as an effective barometer of a material's ability to resist strain-induced distortions [102]. The parameter, initially defined by Kleinman [106], is calculated using the elastic constants, as follows:

$$\zeta = \frac{C_{11} + 8\ C_{12}}{7\ C_{11} + 2\ C_{12}}. \tag{25}$$

The Kleinman parameter ranges from $0 \leqslant \zeta \leqslant 1$ and provides insight into how the atoms of a material shift position under the influence of volume-conserving strain distortions. A ζ value of 0 suggests no internal displacements, while ζ value of 1 and $\frac{1}{2}$ imply that the bond lengths and bond angles, respectively, remain invariant [107]. The lowest extreme limit, $\zeta = 0$, implies that only the volume-conserving component of strain is considered in the calculation. This would be akin to only considering isotropic or hydrostatic pressure changes in the system. The higher extreme limit, $\zeta = 1$, implies that both volume-conserving and shape-changing components of strain are considered equally in the calculation. This case would fully account for anisotropic stresses in the system. The middle limit, $\zeta = 1/2$, is a compromise between the two extremes of $\zeta = 0$ and $\zeta = 1$. It means that both volume-conserving and shape-changing strains are considered, but the volume-conserving strain has a larger contribution. This could be used as a simple approximation for systems where both types of strain play a role but the volume-conserving strain is more important.

Our calculated Kleinman parameters for the UX_2 (X=P, As, Sb) compounds are 0.671, 0.720, and 0.756 for UP_2, UAs_2, and USb_2, respectively. These results are presented in Table 5. The ζ values indicate that the atomic structures of these compounds possess significant rigidity, resisting distortions to their lattice structure. This resilience

implies not just a high degree of internal stability, but also an inherent ability of these materials to withstand external forces or perturbations. Such unique properties, revealed by our analyses, offer new avenues to explore the fundamental physics of these compounds and can prove instrumental in envisioning their potential applications.

In our pursuit of understanding the material properties of the UX_2 (X=P, As, Sb) compounds, we now introduce Pugh's ratio (G/B) into our discussion. This ratio is a well-established metric proposed by Pugh and collaborators to discern the ductility of a material [108]. According to Pugh's theory, materials that have a G/B value larger than 0.57 tend to exhibit brittle behavior, while those with a value smaller than 0.57 tend to behave in a ductile manner [109]. This demarcation provides an intuitive understanding of a material's deformation behavior, which has profound implications for its potential applications.

Upon analyzing the UX_2 (X=P, As, Sb) compounds using this criterion, we observe a fascinating trend. Our computed G/B values, as can be seen in Table 5, sit quite close to the threshold value of 0.57, the border that separates ductile and brittle materials. This intriguing behavior showcases that these compounds embody a delicate balance between brittleness and ductility.

Such an ambivalent material characteristic opens up an exciting area of new physics, potentially offering a unique response to stress and strain. This delicate balance between brittleness and ductility could result in a highly tuneable material response, possibly manifesting novel deformation mechanisms and a range of intriguing properties. This prompts a deeper investigation into the underlying physics that governs the deformability of these compounds, which could hold the key to exploiting their potential in numerous applications.

In the realm of material science, understanding the resistance to volume and shape deformations is a key aspect of studying the mechanical properties of materials. This brings us to the discussion of the bulk modulus (B) and the shear modulus (G), which respectively measure these resistances. The bulk modulus provides insights into the strength of the interparticle bonds and the material's ability to withstand changes in volume. In contrast, the shear modulus conveys the material's responsiveness to shear stress and its resistance to deformation of shape [110].

An essential point to note is that these moduli are not directly measured but inferred from the elastic constants of the material. This is achieved using the Voigt–Reuss–Hill (VRH) approximation, a renowned theoretical framework [111–113]. The VRH approximation provides a way to calculate the effective bulk and shear moduli of a polycrystalline material based on its single-crystal elastic constants, offering upper and lower bounds for these moduli.

This approximation is particularly useful in material science because most engineering materials are polycrystalline in nature. Assuming uniform strain and stress across the polycrystalline material, we can compute the moduli using the polycrystalline modulus average [104, 113]. This approach forms a bridge between the microscopic properties (single-crystal elastic constants) and the macroscopic mechanical properties (bulk and shear moduli), leading to a more comprehensive understanding of the material's mechanical behavior.

This strategy of estimating the bulk and shear moduli of UX_2 (X=P, As, Sb) compounds could unveil new physics phenomena related to their mechanical stability and could potentially provide insights into their potential applications in various technology fields. Let us proceed with the calculations as follows:

$$B = \frac{1}{2}(B_V + B_R), \tag{26}$$

$$G = \frac{1}{2}(G_V + G_R). \tag{27}$$

where B_V, G_V, B_R and G_R are defined in [104] as:

$$B_V = \frac{1}{9}\left[2\,(C_{11} + C_{12}) + C_{33} + 4\,C_{13}\right], \tag{28}$$

$$G_V = \frac{1}{30}(M + 3\,C_{11} - 3\,C_{12} + 12\,C_{44} + 6\,C_{66}), \tag{29}$$

$$B_R = \frac{C^2}{M}, \tag{30}$$

$$G_R = \frac{15}{\left\{(18\,\frac{B_V}{C^2}) + \left[\frac{6}{C_{11}-C_{12}}\right] + (\frac{6}{C_{44}}) + (\frac{3}{C_{66}})\right\}}. \tag{31}$$

where, M and C^2 are $C_{11}+C_{12}+2\,C_{33}-4\,C_{13}$ and $(C_{11}+C_{12})\,C_{33}-2\,C_{13}^2$, respectively.

Our computed values of bulk (B) and shear (G) moduli are presented in Fig. 3. The values of these quantities are also given in Table 5. For all UX_2 (X=P, As, Sb) compounds, B exceeds G, indicating that mechanical strength in these compounds will likely be limited by shear deformation. Among these, UP_2 possesses the largest B and G, followed by UAs_2 and USb_2, suggesting that UP_2 offers the greatest resistance to both volume change and shape deformation. Similarly, UAs_2 demonstrates more resilience against these factors than USb_2.

The Young's modulus (E) and Poisson's ratio (ν) can be computed using the bulk and shear moduli [114–116] as follows:

$$E = \frac{9\,B\,G}{3\,B + G}, \tag{32}$$

$$\nu = \frac{3\,B - 2\,G}{6\,B + 2\,G}. \tag{33}$$

In exploring the mechanical properties of a material, the concepts of Young's modulus (E) and Poisson's ratio (ν) come into play, both of which have deep implications in understanding the material's behavior under deformation.

Young's modulus, a measure of material stiffness, represents the ability of a material to resist changes in length when subjected to longitudinal stress [40,117]. It reflects the intrinsic stiffness of a material's atomic structure, with a higher E indicating greater resistance to deformation, and thus, a stiffer material. In the case of the UX_2 (X=P, As, Sb) compounds, our computed E values are plotted in Fig. 3. The values of these quantities are also given in Table 5. The compound UP_2 demonstrates the highest value of E, indicating superior stiffness and resistance to length changes in comparison to its counterparts. Additionally, UAs_2 exhibits greater stiffness than USb_2, reflecting variations in the rigidity of these compounds.

The concept of Vicker's hardness (H_V) holds paramount importance in material physics, acting as a linchpin to gauge the mechanical resilience of materials. In a study published in July, Rahman et al. [118] delved deeper into superconducting disilicide materials, shedding light on the interplay between structural stability, mechanical properties, and hardness. Just a few months later, in September, Rahman et al. [119] expanded upon this foundational work, turning their focus to La-based superconducting materials, providing crucial insights into the mechanical behaviors, including ductility. Leveraging these investigations, the Vicker's hardness can be defined through the relationship between the bulk modulus and Young's modulus as detailed by Chen et al. [120]:

$$H_V = 2(K^2G)^{0.585} - 3, \tag{34}$$

where $K = G/B$. A key insight is that materials with pronounced hardness inherently resist plastic deformation, serving as bulwarks against external forces. In stark contrast, those characterized by diminished hardness showcase a penchant for plastic deformability, proving invaluable in machining contexts. The demarcation line, as established by Rahman and colleagues, sets a Vicker's hardness value range of 2 to 8 GPa as the benchmark for materials exhibiting both damage-tolerance and machining capabilities [121].

Our investigations into UX_2 (X=P, As, Sb) culminated in detailed H_V values, encapsulated in Table 5. A meticulous analysis of these values, juxtaposed against Rahman's criteria, underscores that while UX_2 (X=P, As) veer towards heightened hardness—aligning them with

Table 6
Transverse (V_T) (Eqs. (41) to (43)) and (b) longitudinal (V_L) (Eqs. (38) to Eq. (40)) elastic wave velocities in different crystal directions and (c) transverse (V_T) (Eq. (35)), longitudinal (V_L) (Eq. (36)) and average (V_{ave}) (Eq. (37)) wave velocities using PBE-GGA+SP+U (U_{eff} = 0.29 Ry), LDA+SP+U (U_{eff} = 0.15 Ry), and LDA+SP+U (U_{eff} = 0.22 Ry) respectively for antiferromagnetic UP_2, UAs_2, and USb_2 in their anti-Cu_2Sb-type tetragonal structure. SP and U_{eff} represent the spin-polarization and effective Hubbard parameter, respectively.

Compound	XCFs	U_{eff} (Ry)	V_L^{100} (m/s)	V_L^{110} (m/s)	V_L^{001} (m/s)	V_{T1}^{100} (m/s)	V_{T1}^{001} (m/s)	$V_{T2}^{1\bar{1}0}$ (m/s)	V_L (m/s)	V_T (m/s)	V_{ave} (m/s)
UP_2	PBE-GGA+SP+U	0.29	5051.879	5727.611	5766.162	3599.123	2983.407	2381.101	5429.810	2998.640	3341.30
UAs_2	LDA+SP+U	0.15	3983.297	4549.232	3820.607	2806.615	2419.564	1745.919	4035.130	2353.340	2610.310
USb_2	LDA+SP+U	0.22	3694.934	4395.179	3591.164	2823.380	2100.486	1518.686	3759.030	2132.210	2370.740

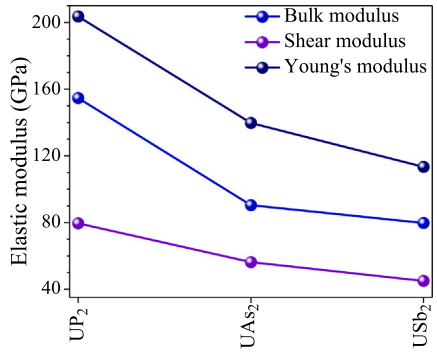

Fig. 3. The bulk modulus (B) (Eq. (26)), shear modulus (G) (Eq. (27)) and Young's modulus (E) (Eq. (32)) using PBE-GGA+SP+U (with U_{eff} = 0.29 Ry), LDA+SP+U (U_{eff} = 0.15 Ry), and LDA+SP+U (U_{eff} = 0.22 Ry) respectively for antiferromagnetic UP_2, UAs_2, and USb_2 in their anti-Cu_2Sb-type tetragonal structure. SP and U_{eff} represent the spin-polarization and effective Hubbard parameter, respectively.

rigorous industrial requirements, USb_2 presents a more nuanced behavior, balancing between damage-tolerance and machinability, a duality often sought in advanced industrial applications.

On the other hand, Poisson's ratio (ν) is a crucial parameter that provides insights into a material's ductility and stability under shear deformation [122]. It is a measure of the material's propensity for plastic deformation, with a larger ν suggestive of enhanced plasticity. Utilizing Frantsevich's rule [123], materials displaying $\nu > \frac{1}{3}$ are classified as ductile, whereas those with $\nu < \frac{1}{3}$ are categorized as brittle.

Interestingly, ν is not only a descriptor of material ductility but can also provide insights into the type of bonding within a compound. For instance, ionic and covalent bonds are often implied by ν values approximating 0.25 and 0.1, respectively [124]. Moreover, central-force interactions within a solid are associated with ν values spanning from 0.25 to 0.50 [125,126].

Our computations for the UX_2 (X=P, As, Sb) compounds reveal ν values that straddle the brittle-ductile threshold, indicating that these compounds exhibit properties intermediate between brittle and ductile behavior. This interesting finding infers the existence of central-force interactions within these compounds. Moreover, the ν values we observed suggest the coexistence of ionic contributions within the bonding structure of these materials, reinforcing their complex physical properties.

In conclusion, our analysis, invoking the concepts of Young's modulus and Poisson's ratio, reveals new physics phenomena pertaining to the mechanical stability and bonding nature of UX_2 (X=P, As, Sb) compounds. This enhanced understanding could pave the way for potential applications in diverse technological fields.

4.2. Acoustic velocity and its anisotropy

The exploration of acoustic properties, particularly sound velocity, in materials constitutes a fundamental domain of research with implications spanning multiple fields. The influence of sound propagation characteristics stretches from the understanding of seismic waves to the creation of musical instruments, underlying the vast applicability of acoustic parameters. In addition to their pivotal role in fields such as material science, geological exploration, and medical diagnostics, these parameters provide a gateway to predicting other critical material properties, like electrical and thermal conductivities [102].

Within the context of our ongoing analysis of the mechanical properties of the UX_2 (X=P, As, Sb) compounds, it is compelling to delve into the study of their acoustic properties. Notably, sound propagation within a material is not uniform, but rather depends on the direction of the propagating wave. Consequently, we categorize sound velocity into three types: transverse (VT), longitudinal (V_L), and average (V_{ave}).

The transverse and longitudinal velocities are representative of the speed of waves propagating perpendicular and parallel, respectively, to the direction of the applied force. In contrast, the average velocity offers a generalized measure of sound speed within the material, independent of the wave's direction.

To compute these velocities, we rely on a set of equations that interlink the acoustic and mechanical attributes of the material [127]. Here, G denotes the shear modulus, B is the bulk modulus, and ρ is the mass density of the material (in kg/m^3):

$$V_T = \left[\frac{G}{\rho}\right]^{\frac{1}{2}}, \tag{35}$$

$$V_L = \left[\frac{3\ B + 4\ G}{3\ \rho}\right]^{\frac{1}{2}}, \tag{36}$$

$$V_{ave} = \left[\frac{1}{3}\left(\frac{1}{V_L^3} + \frac{2}{V_T^3}\right)\right]^{\frac{-1}{3}}. \tag{37}$$

By applying these equations, we are set to calculate the sound velocities for the UX_2 (X=P, As, Sb) compounds under investigation. This analysis is anticipated to contribute to our understanding of their acoustic behavior, enriching our overall study of their physical properties and potential applications.

Understanding the anisotropy of acoustic velocity in a material—a phenomenon that owes its existence to the material's inherent symmetry and the varied directions of wave propagation—offers a deeper insight into the nature of the material [128]. Notably, in the case of materials possessing tetragonal symmetry, this anisotropy is explicitly manifested in the divergent sound velocities along different directions [129]. To examine this effect, we resort to the following mathematical descriptions, which express the longitudinal and transverse sound velocities in terms of the material's elastic constants (C_{11}, C_{12}, C_{33}, C_{44}, and C_{66}) and its mass density (ρ):

$$V_L\,[100] = \sqrt{\frac{C_{11}}{\rho}}, \tag{38}$$

$$V_L\,[001] = \sqrt{\frac{C_{33}}{\rho}}, \tag{39}$$

$$V_L\,[110] = \sqrt{\frac{C_{11} + C_{12} + 2\ C_{66}}{2\ \rho}}, \tag{40}$$

$$V_{T1}\,[001] = \sqrt{\frac{C_{44}}{\rho}}, \tag{41}$$

$$V_{T2}\,[010] = V_{T1}\,[100] = \sqrt{\frac{C_{66}}{\rho}}, \tag{42}$$

$$V_{T2}\left[1\bar{1}0\right] = \sqrt{\frac{C_{11} - C_{12}}{2\ \rho}}. \tag{43}$$

Employing these equations, we are positioned to delve into the investigation of the sound velocities in our target compounds, UX_2 (X=P, As, Sb).

Examining the acoustic velocities of our three compounds of interest—UX_2, with X standing for P, As, or Sb—sheds light on the behavior of acoustic waves within these materials. The anisotropic characteristics of these compounds are clearly manifested in the computed sound velocities provided in Table 6. These insights afford us the opportunity to compare the materials based on their acoustic properties and draw a comprehensive picture of their overall characteristics.

An interesting observation that emerges from our study is the consistently higher speed of longitudinal waves relative to transverse waves across all three materials. This behavior conforms to established principles of wave propagation in anisotropic media, wherein wave speed is contingent on the direction of propagation. Specifically, longitudinal waves—those that traverse parallel to the force direction—generally exhibit higher velocities than their transverse counterparts that propagate perpendicular to the force direction.

A detailed comparison among the studied compounds highlights UP_2 as a particularly compelling material. This compound outshines its counterparts in terms of sound velocities, boasting the fastest speeds for both transverse and longitudinal waves. This indicates efficient sound propagation within UP_2 and suggests superior thermal and electrical conductivities, thus hinting at a wide range of potential applications.

Next in line, UAs_2 demonstrates commendable sound velocities, albeit somewhat reduced compared to UP_2. The larger atomic radius of As in comparison to P might account for this difference, as it may influence the compound's acoustic properties and result in slightly lower wave velocities.

The last compound USb_2 records the slowest velocities for both types of waves among the trio. The substitution of Sb in place of As or P extends the atomic radius even further, likely leading to more pronounced alterations in the compound's acoustic properties, and consequently, slower wave velocities.

Finally, these observations serve as invaluable insights into the acoustic behavior of these compounds, providing indirect indications about their thermal and electrical performance. This integrated understanding not only advances our knowledge about these specific materials but also paves the way for extrapolating their potential for diverse applications, thus emphasizing the importance of a holistic view in materials science research.

4.3. Thermal properties

4.3.1. Debye temperature

The Debye temperature (Θ_D) emerges as a fundamental attribute when exploring the thermal properties of materials. This parameter, named after the Dutch physicist Peter Debye, essentially serves as an indicator of a material's phonon spectrum. It is instrumental in delineating the vibrational behavior within a crystalline solid, thereby contributing significantly to our understanding of the material's dynamic properties.

What makes the Debye temperature particularly crucial is its intimate connection with a host of other physical properties. For instance, there is a notable correlation between Θ_D and a material's melting temperature—a high Debye temperature often implies a high melting point. Similarly, the Debye temperature is intricately tied to thermal conductivity, a key factor dictating how a material transmits heat [102].

Understanding the Debye temperature, therefore, provides a doorway into comprehending the overall thermal behavior of materials. It offers clues about how a material may behave under varying thermal conditions and how effectively it can manage and transport heat. Consequently, insights into Θ_D are invaluable when considering materials for potential applications, particularly those that involve heat management and energy transport. In essence, the Debye temperature serves as a nexus that intertwines multiple physical properties, playing a pivotal role in elucidating the complex physics underlying material behavior.

The Debye temperature, Θ_D, at low temperatures can be accurately determined using the average sound velocity. The relationship between these quantities is expressed by an equation proposed by Schreiber and McMillan [127,130]:

$$\Theta_D = \frac{h}{k_B}\left[\frac{3\ n\ N_A\ \rho}{4\ \pi M}\right]^{\frac{1}{3}} V_m. \tag{44}$$

In this equation, h denotes Planck's constant; k_B represents Boltzmann's constant, which links the energy at the microscopic level with temperature at the macroscopic level; N_A signifies Avogadro's number; ρ is the density of the material; M stands for the molecular weight; and n indicates the number of atoms in a material, an important factor for polyatomic materials. Each of these quantities intricately contributes to shaping the overall phonon behavior of the material, influencing how vibrations propagate within the solid, and thereby impacting its Debye temperature, Θ_D.

This equation elegantly ties together several physical constants and material properties, highlighting the interconnected nature of physics in determining material behavior. It underlines how seemingly disparate quantities—from universal constants to the specific atomic arrangement within a molecule—all converge to determine a single important parameter, the Debye temperature. This parameter not only provides valuable insights into the vibrational characteristics of the material but also hints at several other physical properties, as previously discussed. Thus, through the lens of this equation, we further unravel the intriguing complexities underlying material science.

In a testament to the power of computational analysis in unraveling material behavior, we have successfully determined the Debye temperatures for the compounds UX_2 (X=P, As, Sb). The results of these calculations are meticulously compiled in Table 7 for a comprehensive view.

Of the trio of compounds scrutinized, UP_2 distinguishes itself by exhibiting the highest Debye temperature. This characteristic underscores the potential of this compound to display superior thermal performance. The Debye temperature, as a representation of the phonon energy spectrum of a material, is a critical determinant of thermal conductivity. A higher Debye temperature suggests a broader range of phonon energies, hinting at more efficient phonon transport and hence potentially superior thermal conductivity.

In the descending hierarchy of Debye temperatures, the compound UAs_2 follows the lead set by UP_2. This suggests that while UAs_2 might not match the thermal performance of UP_2, it could still exhibit noteworthy thermal properties owing to its relatively high Debye temperature.

USb_2 claims the last position in this lineup with the lowest Debye temperature among the trio. While this does not dismiss the material's potential in specific applications, it does imply that its thermal properties may not be as impressive as those of UP_2 and UAs_2.

These findings reveal compelling insights into the thermal characteristics of the compounds under study. By correlating these results with our prior analysis of acoustic velocities, we inch closer to a comprehensive understanding of these materials, potentially informing their practical application in diverse scenarios.

Drawing from the intimate correlation between Debye temperature, melting temperature, and thermal conductivity, we can extract some intriguing conclusions regarding the comparative performance of UP_2, UAs_2, and USb_2.

Most notably, the Debye temperature of UP_2, being the highest among the studied compounds, imparts an indication of superior thermal attributes. A higher Debye temperature signals a broader phonon

Table 7
Our calculated Debye temperature (Θ_D) (Eq. (44)), melting temperature (T_m) (Eq. (45)), thermal expansion coefficient (α) (Eq. (46)) and heat capacity (C_P) (Eq. (47)) using PBE-GGA+SP+U (U_{eff} = 0.29 Ry), LDA+SP+U (U_{eff} = 0.15 Ry), and LDA+SP+U (U_{eff} = 0.22 Ry) respectively for antiferromagnetic UP_2, UAs_2, and USb_2 in their anti-Cu_2Sb-type tetragonal structure. SP and U_{eff} represent the spin-polarization and effective Hubbard parameter, respectively.

Compound	Scheme	U_{eff} (Ry)	Θ_D (K)	T_m (K)	$\alpha \times 10^{-5}$ (K^{-1})	C_P $\left(\frac{J}{mol\ K}\right)$
UP_2	PBE-GGA+SP+U	0.29	374.225	1471.669	2.013	74.828
UAs_2	LDA+SP+U	0.15	281.028	1059.530	2.846	74.831
USb_2	LDA+SP+U	0.22	235.284	949.382	3.564	74.832
UP_2	Exp.					79.998[a]
UAs_2	Exp.					79.956[b]
UP_2	Exp.					80.165[c]

[a] Taken from Ref. [27], as measured at 298.15 K.
[b] Taken from Ref. [27], as measured at 298.15 K.
[c] Taken from Ref. [27], as measured at 298.15 K.

energy spectrum, which subsequently results in more efficient phonon-mediated heat transport. Hence, this positions UP_2 favorably to possess a higher melting point and better thermal conduction capabilities than its UAs_2 and USb_2 counterparts.

Moreover, the Debye temperature can be considered a fundamental thermodynamic limit, indicating the highest possible temperature at which the harmonic approximation of phonon behavior remains valid. It implies that a material with a higher Debye temperature is capable of sustaining a wider range of thermal fluctuations while maintaining its structural stability. Thus, it can be inferred that UP_2 may exhibit superior resilience under high-temperature conditions compared to UAs_2 and USb_2.

Progressing further, we can anticipate that UAs_2 would clinch the middle ground in this comparison. Although trailing UP_2, its Debye temperature still surpasses that of USb_2. This suggests that, in terms of melting temperature and thermal conduction capabilities, UAs_2 should outperform USb_2.

These projections, though rooted in the correlation between Debye temperature and other thermal properties, provide a pivotal guidepost for further experimental investigations. They pave the way for a more nuanced understanding of the physics of these materials, thereby aiding the identification of appropriate use-cases based on their thermal properties.

While the theoretical findings we have obtained yield stimulating insights into the thermal characteristics of the UX_2 compounds, it is crucial to view these outcomes through the lens of real-world applications. The theoretical landscape we have traversed primarily provides an idealized picture, which though valuable, does not capture the full complexity of practical scenarios.

The actual thermal behavior of materials in operational conditions can be swayed by a complex confluence of factors that stretch beyond their intrinsic properties. Material purity, for instance, plays a pivotal role in the accurate manifestation of the predicted thermal performance. Impurities, even in small quantities, can introduce scattering centers for phonons, consequently hindering heat transfer and altering the Debye temperature.

Similarly, the fabrication techniques employed to produce the material can significantly shape its thermal behavior. Factors such as grain size, porosity, and lattice defects, all governed by the fabrication process, can influence phonon transport, thereby affecting the overall thermal properties.

Furthermore, operating conditions such as ambient temperature, pressure, and the presence of electromagnetic fields could potentially modulate the thermal performance of these compounds. Such conditions can impact the phonon population and their interactions, thereby influencing heat transport.

Given this rich tapestry of factors that influence the thermal behavior of materials, it is clear that our theoretical findings form just one part of the story. Therefore, experimental validation becomes a crucial next step to corroborate these predictions and gain a comprehensive understanding of these compounds' thermal performance.

Moreover, additional analysis integrating the impact of the above-mentioned extrinsic factors can provide a more realistic picture of the thermal behavior. This holistic approach, embracing both the intrinsic properties predicted by our theoretical framework and the extrinsic influences typical in practical scenarios, will provide a more nuanced understanding of these compounds, thereby informing their potential applications more effectively.

4.3.2. Melting temperature

The melting temperature (T_m) serves as a pivotal physical attribute that significantly delineates the characteristics of materials. Its value directly delineates a material's capacity to withstand high temperatures, an essential criterion for applications that function under extreme thermal conditions, including various facets of the energy, aerospace, and automotive industries.

One approach to estimate the melting temperature leverages the elastic constants of the material. Elastic constants, which provide a measure of a material's resistance to deformation under an applied force, contribute to many of the material's macroscopic properties, including its melting temperature. By correlating these constants to T_m, we gain an accessible pathway to infer this critical parameter.

Specifically, a methodology pioneered by Fine et al. enables us to estimate the melting temperature of materials exhibiting tetragonal symmetry by exploiting their respective elastic constants [131]. This approach takes into consideration the interplay between the elasticity of the material and its response to heat, essentially capturing how the lattice vibrations evolve with increasing temperature until reaching the point of structural collapse—the melting point.

The equation provided by Fine et al. is as follows:

$$T_m = 354\ \mathrm{K} + \left(4.5\ \frac{\mathrm{K}}{\mathrm{GPa}}\right)\left[\frac{2C_{11}\ (\mathrm{GPa}) + C_{33}\ (\mathrm{GPa})}{3}\right] \pm 300\ \mathrm{K}. \quad (45)$$

This equation amalgamates the averaged influence of the C_{11} and C_{33} elastic constants, scaled by a factor derived from empirical analysis, into a baseline temperature. The resulting value, while offering an initial estimation, does come with an uncertainty of ±300 K to account for the variability in the melting behavior of different materials. This approach effectively bridges the gap between the microscopic elastic properties of a material and its macroscopic thermal behavior, rendering a tool to predict melting temperatures.

Building upon our calculations, we have been able to extract estimates for the melting temperatures of the compounds UX_2, where X represents either P, As, or Sb. These results, collated in Table 7, add another dimension to our understanding of these materials, painting a more detailed picture of their thermal resilience and utility in high-temperature settings.

Observing the estimated melting temperatures, it becomes evident that these materials are not just academically interesting, but could also hold substantial promise for practical applications demanding substantial thermal resistance. Such resilience could make them viable contenders in a range of high-temperature applications across a spectrum of industries and research disciplines.

For instance, these compounds could potentially contribute to the domain of energy production, where materials capable of withstanding extreme heat are essential for various processes, including nuclear reactions or thermoelectric power generation. Similarly, in the manufacturing sector, materials with high melting points are often needed in mold-making, metal casting, and other processes involving high-temperature operations.

Furthermore, these compounds may present intriguing possibilities for further exploration within the realm of materials science itself. Their properties could stimulate new theoretical and experimental research paths, paving the way for novel materials or alloys with optimized thermal characteristics.

The realization of such applications, however, necessitates thorough experimental validation and practical assessment of these compounds under real-world conditions, a challenging yet exciting prospect for further studies.

In addition to the broader applications, our study has also shed light on the impact of sequential pnictogen replacement within the UX_2 compounds, transitioning from P to As, and then from As to Sb. An intriguing trend emerged from this investigation: the melting temperature of these compounds tended to diminish in response to this sequential substitution.

Exploring this observation further, it is notable that the change in pnictogen atom is not merely a chemical alteration. It also introduces a variation in the lattice structure of the material. As we shift from P to As, and subsequently from As to Sb, the lattice parameter—a crucial factor in defining the material's physical properties—experiences an increase.

Interestingly, this systematic growth in the lattice parameter appears to be intimately linked to the observed reduction in the melting temperature. This connection could be rooted in the influence of the lattice parameter on the strength of the bonding within the crystalline structure. A larger lattice parameter could lead to weaker atomic interactions, which in turn would lower the energy required to overcome these bonds—thus lowering the melting temperature.

While this explanation offers a promising perspective, it is a hypothesis based on our current understanding and computational findings. The intriguing interplay of atomic substitution and lattice parameter variation, and their effect on the thermal properties of these materials, points to an area ripe for deeper investigation. Further theoretical and experimental studies could significantly enrich our comprehension of these effects, opening new vistas in the realm of materials physics.

Our observations regarding the linked alterations in melting temperature and lattice parameter underscore a fundamental aspect of materials physics: the intricate connection between a compound's structural attributes and its thermal properties. This entwined relationship demonstrates how alterations in the microscale atomic structure can manifest as significant changes in macroscale physical properties.

This elucidation carries profound implications for the design and creation of new materials. By understanding and harnessing this interconnection, we can potentially guide the structural configuration of a compound to yield specific thermal characteristics. For instance, the methodical manipulation of lattice parameters or the careful selection of substituent atoms could enable us to engineer materials with tailored thermal properties—a capability that could have far-reaching impact across various fields such as energy storage, thermoelectric devices, and heat-resistant materials.

This understanding expands the horizon of 'material by design' philosophy in the realm of new physics, a philosophy that could revolutionize how we approach the synthesis and application of materials in the future. It empowers us to move beyond traditional trial-and-error based methods, towards a more structured, predictive approach that is rooted in a comprehensive understanding of the microscopic–macroscopic link. Therefore, our study underscores the importance of continual advancements in computational physics, alongside experimental confirmations, to decode the fascinating 'materials universe'.

While our analysis has shed significant light on the correlation between lattice parameters and melting temperature in the UX_2 compounds, it is crucial to acknowledge that this relationship is likely to be a part of a more complex picture. Our findings represent an important milestone in understanding these materials, yet they also underscore the need for further exploration to validate and deepen our understanding of the underlying mechanisms.

A myriad of factors might contribute to the trends we observed, and our study has mainly focused on the alterations induced by lattice parameter changes. However, in the realm of material physics, the behavior of compounds often springs from an intricate interplay of numerous factors. Aspects such as electronic configurations, bonding characteristics, and structural stability might also have a significant role in this context. Each of these factors could exert influence on the thermal properties of the compounds, either independently or through interaction with other parameters.

For instance, the electronic configuration could impact the nature and strength of bonds formed within the material, and consequently influence its thermal and mechanical properties. Similarly, the inherent structural stability of the compound could have implications for its resilience to thermal stress and thereby impact its melting temperature. Understanding these associations could reveal more nuanced and holistic insights into the behavior of these compounds.

Therefore, while our study provides a valuable stepping-stone, comprehensive exploration of these other potential influencing factors warrants attention in future research. This could be achieved through an amalgamation of experimental and additional theoretical studies, leveraging advanced methodologies in both domains. This holistic approach will help unravel the rich tapestry of relationships that govern the properties of these materials, aiding in the development of a more complete and accurate physical model. Such advances will undoubtedly further the field of new physics and material design, propelling us closer to the frontier of knowledge in these areas.

4.3.3. Thermal expansion and heat capacity

In the realm of materials science, gaining a comprehensive understanding of a material's properties often necessitates studying its thermodynamic characteristics. Among these characteristics, the thermal expansion coefficient (α) and heat capacity (C_P) hold particular importance. These parameters serve as crucial indicators of how a material responds to variations in temperature and can provide valuable insight into its fundamental physical behavior [102].

The thermal expansion coefficient (α) essentially quantifies how a material's size changes as a response to a shift in temperature. In other words, it represents the extent to which the material expands or contracts per unit temperature change. This parameter is instrumental in understanding the material's dimensional stability under thermal fluctuations and can be crucial in applications where material stability under thermal stresses is a critical concern.

Meanwhile, the heat capacity (C_P) is a measure of the amount of heat a material can absorb per unit change in temperature. This property gives us a sense of how the material handles thermal energy—whether it gets hot quickly or is efficient at dissipating heat. It is a vital parameter in predicting the material's thermal behavior and can be tied to other properties such as melting temperature and thermal conductivity.

Together, these properties serve as an index to a material's thermal stability and performance. Comprehensive understanding of these parameters is essential in exploring the potential applications of materials, especially in scenarios that demand superior thermal management, such as energy storage and conversion, electronics, and manufacturing processes [102]. The intricate interplay of these thermodynamic properties brings to light fascinating aspects of new physics, further enriching our knowledge of material behavior under thermal conditions.

An integral parameter in thermodynamics, the thermal expansion coefficient (α), provides insights into the volumetric changes a material undergoes as it experiences temperature shifts. In essence, it encapsulates the degree to which a material expands or contracts in response to each degree of temperature change. This property has fundamental implications for the material's response to thermal stress and its dimensional stability under varied thermal conditions. The thermal expansion coefficient can be computed using an empirical relationship given by Ashby [132]:

$$\alpha = \frac{1.6 \times 10^{-3}}{G}. \tag{46}$$

In this equation, G represents the shear modulus of the material, which is a measure of its rigidity or resistance to shape change under shear stress. This relationship illustrates a fascinating aspect of physics: the coupling between mechanical and thermal properties of materials. The fact that a mechanical characteristic, such as the shear modulus, can influence a thermal property, like the thermal expansion coefficient, reveals the intricate interplay of physical parameters within a material. This interdependence emphasizes the need for a comprehensive understanding of various physical properties to accurately predict the material's behavior under diverse operating conditions. It also underscores the emergence of new physics within the realm of material science, demonstrating how fundamental properties intersect and interact, thereby shaping the overall performance of materials.

The computational analysis of the thermal expansion coefficient (α) for the UX_2 compounds (where X represents P, As, or Sb) has been tabulated in Table 7. Interestingly, a discernible trend emerges when substituting the pnictogen atoms in UX_2, from P to As and subsequently to Sb. Each of these substitutions leads to a consistent increase in the thermal expansion coefficient, indicating that the volumetric expansion of these compounds becomes more sensitive to temperature changes as we progress from P to Sb.

This observed trend aligns well with the known inverse correlation between thermal expansion coefficient and melting temperature, described mathematically by the relationship $\alpha \approx \frac{0.02}{Tm}$ [131,132]. Consequently, the aforementioned increase in α resonates with the earlier noted decrease in melting temperatures upon progressing from UP_2 to UAs_2 and USb_2, reaffirming the interconnected nature of these thermophysical properties.

This pattern signifies the inherent interplay between a material's thermal and structural attributes, contributing to the overall picture of how replacing the pnictogen atom affects the compound's behavior. By understanding these shifts, we can better predict and possibly manipulate the performance of these materials under various thermal conditions, underscoring the emergent complexity in this area of materials physics.

The heat capacity per unit volume, denoted by $\rho\, C_P$, is a valuable thermophysical quantity that signifies a material's ability to accumulate thermal energy. This parameter often correlates directly with thermal conductivity, such that materials with higher heat capacities are generally better conductors of heat [102]. Consequently, knowledge of the heat capacity can offer critical insights into a material's thermal performance and inform decisions regarding its suitability for various applications, particularly those requiring efficient thermal management. The heat capacity per unit volume can be determined as per the equation provided by Ashby [132]:

$$\rho C_P = \frac{3k_B}{\Omega} (\mathrm{J/m^3K}). \tag{47}$$

Here, k_B denotes Boltzmann's constant, while Ω represents the atomic volume. The equation essentially translates to the fact that the heat capacity is related to the atomic configuration of the material, more specifically the number of atoms per unit volume ($N = 1/\Omega$).

In the case of the UX_2 compounds under investigation, we have performed computational analyses to determine the heat capacity values. These findings are summarized in Table 7. Interestingly, the heat capacity data exhibit an encouraging agreement with available experimental data from the literature, thus strengthening the validity of our computational approach [27].

This harmonization between our calculated values and empirical results not only provides assurance of our methodology but also underlines the fundamental relationship between the microstructure of materials (i.e., atomic volume and density) and their macroscopic thermal properties. Such insights are invaluable in paving the way for further research into the new physics underlying material behavior, enabling the fine-tuning of thermal characteristics for desired applications.

The collective outcomes of our study, especially those pertaining to the thermal expansion coefficient and heat capacity of the UX_2 compounds, serve to enrich the overall thermophysical profile of these materials. Our investigations have shed light on the intrinsic thermal characteristics of these compounds, enabling us to predict their behavior under temperature changes, an attribute integral to various practical applications.

The findings on thermal expansion illustrate how these materials respond volumetrically to temperature variations. Simultaneously, the determination of heat capacity illuminates their inherent capacity to store thermal energy. Both these attributes are key factors that influence a material's performance in terms of its thermal management capabilities.

Such comprehensive analysis, underpinned by the principles of new physics, provides invaluable insights, not only expanding our understanding of these specific materials but also serving as a potential guide for future research on materials with similar structures. Ultimately, the goal is to relate these fundamental thermal characteristics to practical applications, enhancing the performance and reliability of devices in various sectors, ranging from energy production to advanced manufacturing.

This scientific endeavor of piecing together disparate thermal properties into a cohesive thermophysical profile is an integral step towards understanding the complex interplay of various material attributes, further bridging the gap between theoretical predictions and real-world material performance.

4.3.4. Minimum thermal conductivity

The property of thermal conductivity holds a significant place in the realm of material science, chiefly due to its governing role in dictating a material's proficiency in transferring thermal energy. Such a trait gains prominence in numerous applications where the management of heat flow becomes a critical factor, for instance, in the realm of electronic devices where controlling thermal dissipation is essential to maintain optimal functionality, or in the context of thermal insulation materials, where efficient impedance of heat flow is desired.

The thermal conductivity of a material does not remain constant across the entire temperature spectrum. As a material's temperature crosses the Debye temperature, a notable phenomenon is often observed where its thermal conductivity descends and eventually plateaus to a relatively constant value. This ascertained lower limit, often recognized as the minimum thermal conductivity (k_{min}), holds particular interest in the study of material thermal behavior. The existence of this minimum thermal conductivity threshold, extensively documented in previous research [102], suggests a limitation to the heat-carrying capacity of the phonons within the material, introducing fascinating implications to the broad area of heat transport in condensed matter physics.

The concept of minimum thermal conductivity gains quantifiable meaning through the application of the Debye model, with the pioneering work by Clarke providing a fundamental mathematical construct [133]. According to Clarke's model, the minimum thermal conductivity (k_{min}) can be expressed by the following relationship:

$$k_{min} = k_B\, V_{ave}\, (V_{atomic})^{\frac{-2}{3}}. \tag{48}$$

In this representation, k_B denotes the Boltzmann constant, encapsulating the essence of the fundamental link between temperature and energy. V_{ave} signifies the average sound velocity within the material, emphasizing the critical role of phononic transport properties in the thermal behavior of the material. Lastly, V_{atomic} denotes the cell volume per atom, pointing towards the significance of atomic scale structure and arrangement in mediating heat transport.

By establishing this relation, we can comprehend the multifaceted interplay between atomic structures, phononic properties, and the resulting thermal conductivity of a material. This understanding grants us a more nuanced perspective on the intrinsic and structural influences on heat transfer mechanisms within solid-state materials, shedding light on the complex web of interactions that make up the microscopic world of thermal physics.

The outcomes derived from our computational frameworkframework, as shown in Fig. 4, indicate a strong correlation between the minimum thermal conductivity (k_{min}), sound velocities, and the Debye temperatures (Θ_D) of the considered materials. We observe a clear trend where materials that possess higher sound velocities and Debye temperatures tend to display correspondingly higher values of k_{min}.

This result not only corroborates our initial expectations but also serves as a testament to the validity of our computational model. It exemplifies the effective transfer of vibrational energy through phonons in materials exhibiting higher sound velocities and Debye temperatures, thus justifying the observed elevated thermal conductivities. This trend is an embodiment of the intricate connections between the macroscopic thermal behaviors of materials and their underlying microscopic phononic characteristics.

In essence, our computational investigations elucidate the crucial role played by sound velocities and Debye temperatures in dictating the thermal performance of materials, providing a quantitative measure of how thermal transport is intrinsically linked to these fundamental properties.

Drawing specific examples from our analysis, we observe an interesting trend within the UX_2 compounds, where X encompasses P, As, and Sb. Notably, UP_2, distinguished by its superior sound velocity and higher Debye temperature (Θ_D), demonstrates the greatest minimum thermal conductivity (k_{min}) among the considered compounds. This highlights the material's efficiency in thermal energy transfer, which is inherently governed by its distinct phononic properties.

On descending the order of thermal performance, UAs_2 follows next, and subsequently, USb_2. This indicates a discernible relationship between the thermal properties under consideration and the atomic makeup of the material. Intriguingly, the change in pnictogen atoms from P to As and from As to Sb across these compounds impacts the atomic scale vibrational characteristics, thus affecting the macroscopic thermal response of these materials.

To summarize, this observed trend underscores the complex interplay between the atomic configuration of these compounds and their thermal attributes, demonstrating how variations at the atomic level can dramatically alter the material's bulk thermal properties. The potential ramifications of these findings could extend to the design and synthesis of materials with tailored thermal characteristics, catering to specific application requirements in numerous domains of science and technology.

The nuances of thermal conductivity extend beyond scalar properties, as it is a manifestation of intricate transport phenomena in solids. Consequently, the directional considerations play a critical role in determining its value, rendering thermal conductivity an anisotropic property. This anisotropy means that the efficiency of heat transfer may vary significantly depending on the specific path it follows through the material. This concept is of paramount importance in materials science and engineering, particularly when dealing with applications where the orientation of heat flow is of crucial relevance.

The root of this anisotropy lies within the material's intrinsic vibrational characteristics, especially the phononic velocities. In particular, the average sound velocity (V_{ave}) inherently depends upon the orientation-dependent longitudinal and transverse sound velocities (V_L and V_T), suggesting an inherent link between the anisotropy in sound velocities and the thermal conductivity.

Therefore, the resulting anisotropy in minimum thermal conductivity (k_{min}) can be seen as a direct consequence of the orientation-dependent nature of these sound velocities. A deeper comprehension of this relationship presents a new vista to understand and manipulate thermal transport mechanisms, bringing us a step closer to engineering materials with bespoke anisotropic thermal properties.

The exploration of thermal conductivity anisotropy has been given a robust mathematical footing with the advent of the Cahill and Clarke model. This model extends the conventional perspective by incorporating the directional dependence of thermal conductivity, thereby providing a more comprehensive understanding of heat transport mechanisms in solids [134]. The cornerstone of this model is the equation:

$$k_{min} = \frac{k_B}{2.48}\, n^{\frac{2}{3}}\, (V_L + V_{T1} + V_{T2}), \tag{49}$$

which enables the calculation of the minimum thermal conductivity in different crystallographic directions. In this formulation, k_B represents the Boltzmann constant, while V_L, V_{T1}, and V_{T2} are the longitudinal and the two transverse sound velocities, respectively.

Importantly, the model also introduces the concept of atomic packing in a unit cell, captured by the parameter n, the number of atoms per unit volume. This is determined by the total number of atoms (N) in the unit cell and the cell volume (V), denoted as $n = \frac{N}{V}$.

The prominence of n in the equation signals the significance of the atomic arrangement within the lattice, as it critically impacts the thermal behavior of the material. Consequently, this model not only helps understand the anisotropy in thermal conduction but also links this phenomenon to the very essence of the material's crystalline structure, bridging the gap between structural characteristics and macroscopic thermal properties.

The anisotropic nature of thermal conductivity for the UX_2 compounds, as shown in Fig. 4, reveals intriguing nuances in the heat conduction properties, with calculated minimum thermal conductivities demonstrating distinct values along the [100], [001], and [110] crystallographic directions.

Remarkably, it is observed that UP_2 consistently outperforms UAs_2 and USb_2 in terms of k_{min} across all the evaluated crystallographic orientations. This strongly indicates a profound impact of the atomic constitution of the material on its anisotropic heat conduction behavior, thereby underlining the importance of the elemental makeup in tuning the thermal properties.

Furthermore, an intriguing characteristic emerges when comparing the anisotropic thermal conductivities with the isotropic k_{min}. The findings reveal that, irrespective of the specific compound under consideration, the minimum thermal conductivity along these directions consistently exceeds the isotropic k_{min}, thus shedding light on a potential avenue for optimizing heat conduction.

These findings present a compelling case for the role of crystallographic orientation in modulating the thermal conductivity of materials, which might have far-reaching implications in the design and application of these materials, particularly in domains necessitating superior thermal management capabilities. Thus, the study not only elucidates the fundamental physics of heat transfer but also paves the way for practical advancements in materials design.

4.4. Elastic anisotropy

A material's mechanical properties often exhibit directional dependence, a phenomenon known as elastic anisotropy. Elastic anisotropy, in turn, influences several crucial physical properties of materials such as the formation and propagation of micro-cracks, the evolution of plastic deformations, and so on [102]. Therefore, the understanding of elastic anisotropy holds significant value, particularly in engineering

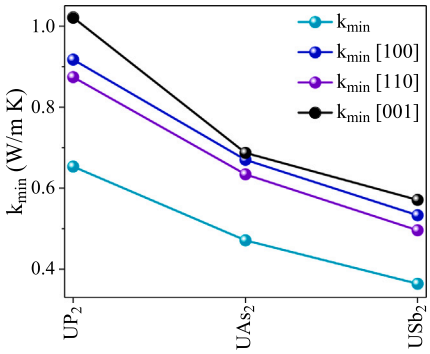

Fig. 4. The minimum thermal conductivity (k_{min}) (Eq. (48)) along different directions (Eq. (49)) using PBE-GGA+SP+U (U_{eff} = 0.29 Ry), LDA+SP+U (U_{eff} = 0.15 Ry), and LDA+SP+U (U_{eff} = 0.22 Ry) respectively for antiferromagnetic UP_2, UAs_2, and USb_2 in their anti-Cu_2Sb-type tetragonal structure. SP and U_{eff} represent the spin-polarization and effective Hubbard parameter, respectively.

science where material behavior under different load orientations is critical [135].

An effective way of quantifying anisotropy in materials is through a universal anisotropy factor. Ranganathan and Ostoja-Starzewski [136] proposed an equation to calculate this factor:

$$A^U = 5\frac{G_V}{G_R} + \frac{B_V}{B_R} - 6 \geq 0. \tag{50}$$

In this equation, G_V and G_R represent the Voigt and Reuss shear moduli, respectively, while B_V and B_R represent the Voigt and Reuss bulk moduli, respectively. The Voigt modulus represents an upper bound and the Reuss modulus a lower bound on the effective elastic modulus of a material. Therefore, the ratio of these moduli in the equation provides a measure of the anisotropy of the material. A higher value of A^U signifies a greater degree of anisotropy in the elastic properties.

Chung and Buessem [137] proposed additional measures to quantify the anisotropy in compression (A_B) and shear (A_G). These are defined by the following equations:

$$A_B = \frac{B_V - B_R}{B_V + B_R}, \tag{51}$$

and :

$$A_G = \frac{G_V - G_R}{G_V + G_R}. \tag{52}$$

These formulas are used to calculate the degree of anisotropy. For an isotropic compound, A^U, A_B, and A_G should all equate to zero. Any deviation from this value suggests a degree of anisotropy in the material [102].

Our calculated A^U, A_B, and A_G values for UX_2 (X=P, As, Sb) are presented in Table 8. As can be seen, A^U deviates from zero in all the compounds under study. This indicates an anisotropic behavior within these materials. Similarly, the nonzero values of A_B and A_G point to anisotropy in compression and shear, respectively, within the UX_2 (X=P, As, Sb) compounds.

Moreover, anisotropy in shear (A_G) is larger than the anisotropy in compression (A_B), as evidenced by their respective values. The USb_2 compound exhibits the highest anisotropy values A^U, A_B, and A_G compared to the two other UX_2 (X=P, As) compounds. The UAs_2 compound shows the second-highest anisotropy values compared to UP_2.

Another critical element derived from elastic constants is the shear anisotropic factors, which measure the degree of anisotropy in the bonding between atoms of a compound across different planes. Within tetragonal symmetry, three distinct shear anisotropic factors exist [138, 139], as defined by the following equations:

$$A_1 = \frac{4\ C_{44}}{C_{11} + C_{33} - 2\ C_{13}}, \tag{53}$$

$$A_2 = \frac{4\ C_{55}}{C_{22} + C_{33} - 2\ C_{23}}, \tag{54}$$

$$A_3 = \frac{4\ C_{66}}{C_{11} + C_{22} - 2\ C_{12}}. \tag{55}$$

In these equations, A_1, A_2, and A_3 represent the shear anisotropic factors for the (100), (010), and (001) shear planes, respectively. For compounds exhibiting isotropy in atomic bonding across different planes, the values of A_1, A_2, and A_3 should be equal to 1. Any deviation from this value signifies anisotropy [138,139].

Our calculations for A_1, A_2, and A_3 values in the compounds UX_2 (X=P, As, Sb) are provided in Table 8. These values deviate from 1, confirming anisotropy in the shear along the [100], [010], and [001] directions. The (100) shear plane shows the highest shear anisotropic factor across all studied compounds. In terms of individual compounds, USb_2 exhibits the most significant shear anisotropic factor for the (100) shear plane, followed by UAs_2 and then UP_2. In the case of tetragonal compounds, the linear compressibility along the a and c axes can be calculated using the following formulas as proposed by Milman et al. [140]:

$$\beta_a = \frac{C_{33} - C_{13}}{D}, \tag{56}$$

$$\beta_c = \frac{C_{11} + C_{12} - 2\ C_{13}}{D}. \tag{57}$$

In these equations, D represents the term $(C_{11} + C_{12})C_{33} - 2C_{13}^2$. Using these formulations, we have computed the values of β_a and β_c for the compounds UX_2 (X=P, As, Sb), as presented in Table 8.

Our calculations indicate that for all these UX_2 compounds, both β_a and β_c values are relatively small, signifying low compressibility along the a and c axes. However, a closer examination reveals that the compressibility along the a axis is marginally lower than that along the c axis for these compounds.

In the context of elastic calculations, the transformation of compliance for a material from the reference system, denoted as S_{ijkl}, to the distorted system, denoted as $S'_{\alpha\beta\gamma\delta}$, can be described through a specific relationship. Marmier et al. [141] defines this transformation as follows:

$$S'_{\alpha\beta\gamma\delta} = a_{\alpha i}a_{\beta j}b_{\gamma k}b_{\delta l}S_{ijkl}. \tag{58}$$

This equation involves two vectors, **a** and **b**, the coordinates of which can be represented as:

$$\mathbf{a} = \begin{pmatrix} sin\theta\ cos\varphi \\ sin\theta\ sin\varphi \\ cos\theta \end{pmatrix}; 0 \leq \theta \leq \pi, 0 \leq \varphi \leq \pi, \tag{59}$$

$$\mathbf{b} = \begin{pmatrix} cos\theta\ cos\varphi\ cos\gamma - sin\theta\ sin\gamma \\ cos\theta\ sin\varphi\ cos\gamma - cos\theta\ sin\gamma \\ -sin\theta cos\gamma \end{pmatrix}; 0 \leq \gamma \leq 2\pi. \tag{60}$$

These vectors are key to understanding the transformation between the reference and distorted compliance systems.

Utilizing Eq. (58), we can establish the spatial dependence of several key material properties: linear compressibility (β), Young's modulus (E), shear modulus (G), and Poisson's ratio (ν). These can be defined along (xy), (xz), and (yz) planes as follows [141]:

$$\beta(\theta,\varphi) = \frac{1}{B} = a_i a_j S_{ijkk}, \tag{61}$$

$$E(\theta,\varphi) = \frac{1}{S'_{11}(\theta,\varphi)} = \frac{1}{a_i a_j a_k a_l S_{ijkl}}, \tag{62}$$

$$G(\theta,\varphi,\gamma) = \frac{1}{4S'_{66}(\theta,\varphi,\gamma)} = \frac{1}{4}\frac{1}{a_i b_j a_k b_l S_{ijkl}}, \tag{63}$$

$$\nu(\theta,\varphi,\gamma) = -\frac{S'_{12}(\theta,\varphi,\gamma)}{S'_{11}(\theta,\varphi)} = -\frac{a_i a_j b_k b_l S_{ijkl}}{a_i a_j a_k a_l S_{ijkl}}. \tag{64}$$

Table 8
Universal anisotropy factor (A^U) (Eq. (50)), anisotropy in compression (A_B) (Eq. (51)), anisotropy in shear (A_G) (Eq. (52)), shear anisotropic factors (A_1, A_2 and A_3) (Eqs. (53), (54) and (55), respectively) and linear compressibilities (β_a and β_c using Eqs. (56) and (57), respectively) (GPa^{-1}) considering PBE-GGA+SP+U (U_{eff} = 0.29 Ry), LDA+SP+U (U_{eff} = 0.15 Ry), and LDA+SP+U (U_{eff} = 0.22 Ry) respectively for antiferromagnetic UP_2, UAs_2, and USb_2 in their anti-Cu_2Sb-type tetragonal structure. SP and U_{eff} represent the spin-polarization and effective Hubbard parameter, respectively.

Compound	XCFs	U_{eff} (Ry)	A^U	A_B	A_G	A_1	A_2	A_3	β_a	β_c
UP_2	PBE-GGA+SP+U	0.29	0.383	0.002	0.036	2.285	0.984	0.687	0.002	0.002
UAs_2	LDA+SP+U	0.15	0.604	0.016	0.054	2.584	1.031	0.743	0.003	0.005
USb_2	LDA+SP+U	0.22	0.933	0.015	0.083	3.456	0.936	0.553	0.003	0.006

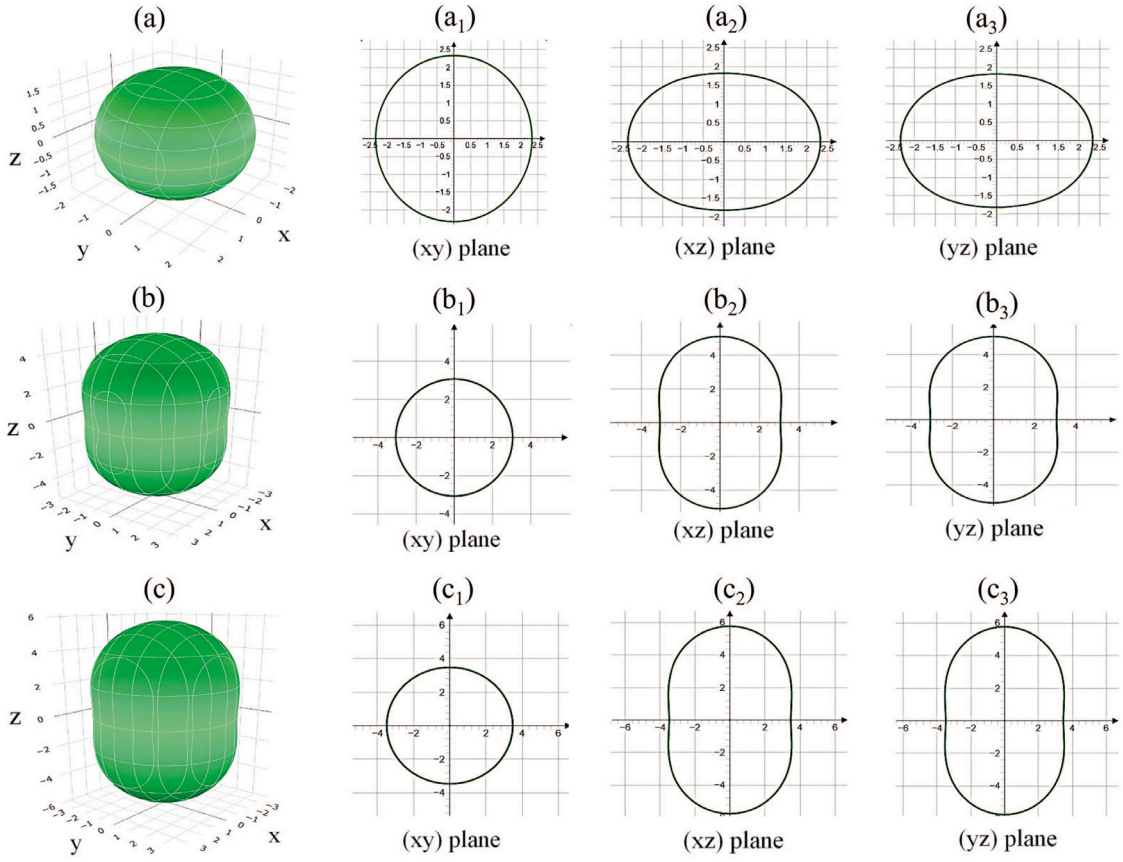

Fig. 5. Spatial dependence of linear compressibilities calculated by Eq. (61) using the PBE-GGA+SP+U (U_{eff} = 0.29 Ry), LDA+SP+U (U_{eff} = 0.15 Ry), and LDA+SP+U (U_{eff} = 0.22 Ry) for antiferromagnetic (a) UP_2, (b) UAs_2 and (c) USb_2 in their anti-Cu_2Sb-type tetragonal structure and their projections on (a_1), (b_1), and (c_1) (xy) plane, (a_2), (b_2), and (c_2) (xz) plane, and (a_3), (b_3), and c_3 (yz) plane, respectively. SP and U_{eff} represent the spin-polarization and effective Hubbard parameter, respectively.

Here, S_{ij} denotes the elastic compliance constant, a tensor that quantifies the deformation a material experiences under applied stress. The a, b, and c directions of the lattice correspond to the direction cosines l_1, l_2, and l_3, respectively.

Let us explore the spatial variations in linear compressibility (β) for three distinct materials: UP_2, UAs_2, and USb_2. The measurements were taken under three separate conditions, including PBE-GGA+SP+U with U_{eff} = 0.29 Ry, LDA+SP+U with U_{eff} = 0.15 Ry, and LDA+SP+U with U_{eff} = 0.22 Ry. These conditions represent different computational approaches to density functional theory (DFT), which are utilized in the calculation of electronic structure properties.

Linear compressibility is a crucial mechanical property, quantifying the deformation of a material under uniaxial stress. It is noteworthy that linear compressibility varies spatially for these materials, an insight that emerges from Fig. 5. This observation demonstrates the anisotropic nature of the linear compressibility in these materials, signifying that their mechanical response to uniaxial stress can significantly differ based on the direction of the applied stress.

In Fig. 5, each material is represented along the three crystallographic planes: (xy), (xz), and (yz). These planes are demonstrated for each material in Figs. 5 (a1, b1, and c1), (a2, b2, and c2), and (a3, b3, and c_3), respectively. This comprehensive representation provides a holistic understanding of the spatial variation of linear compressibility under various conditions and material configurations. It also underscores the anisotropy of these materials, a crucial factor to consider when predicting their behavior under stress in different directions.

This analysis of spatial variation and anisotropy in linear compressibility is a significant contribution to our understanding of the mechanical properties of UP_2, UAs_2, and USb_2. These insights could be instrumental in leveraging these materials in technological applications where their response to applied stress is of critical importance.

Let us delve deeper into the observed anisotropic properties of linear compressibility (β) for the materials UP_2, UAs_2, and USb_2. Anisotropy, in this context, indicates that the linear compressibility of these materials is not uniform in all directions but varies depending on the axis along which it is evaluated. This anisotropic behavior has significant implications for the materials' physical and mechanical properties, especially in response to applied forces.

Linear compressibility (β) is inversely related to the bulk modulus (B), as indicated by Eq. (61). The bulk modulus is a measure of a substance's resistance to uniform compression—it quantifies the degree to which a substance will deform (compress or expand) under

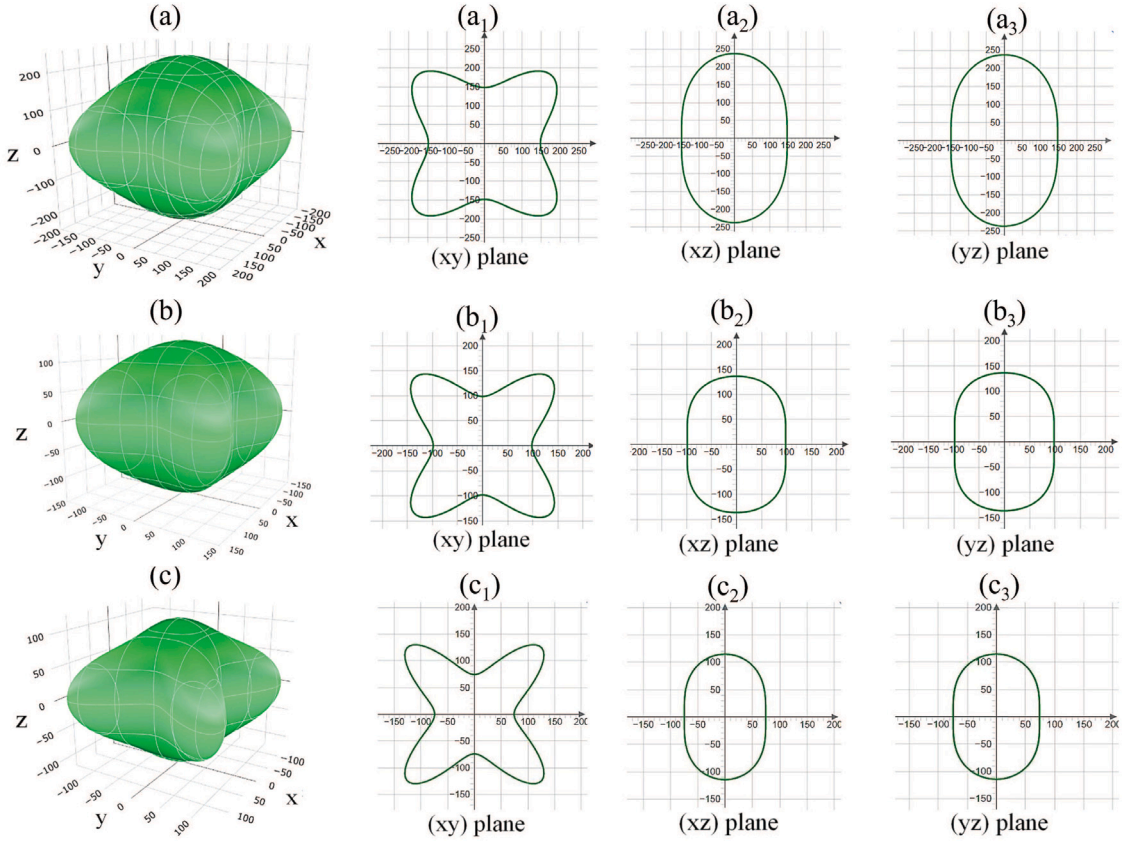

Fig. 6. Spatial dependence of Young's moduli calculated by Eq. (62) using the PBE-GGA+SP+U (U_{eff} = 0.29 Ry), LDA+SP+U (U_{eff} = 0.15 Ry), and LDA+SP+U (U_{eff} = 0.22 Ry) for antiferromagnetic (a) UP_2, (b) UAs_2 and (c) USb_2 in their anti-Cu_2Sb-type tetragonal structure and their projections on (a_1), (b_1), and (c_1) (xy) plane, (a_2), (b_2), and (c_2) (xz) plane, and (a_3), (b_3), and c_3 (yz) plane, respectively. SP and U_{eff} represent the spin-polarization and effective Hubbard parameter, respectively.

applied pressure. Given this inverse relationship, if a material exhibits anisotropy in its linear compressibility, this implies a corresponding anisotropy in its bulk modulus.

In the context of the UX_2 compounds (where X=P, As, Sb), this suggests that their bulk moduli—and thus their resistance to uniform compression—differ depending on the direction of the applied pressure. This underscores a key aspect of the materials' structure: the bond strength between the constituent particles and their resistance to changes in volume exhibit direction-dependent, anisotropic behavior.

Anisotropy in bulk modulus can lead to different deformations in response to the same stress applied along different axes, which has considerable implications for the design and utilization of these materials in practical applications. Understanding the anisotropy can help to anticipate the materials' performance under various loading conditions, providing valuable insights for their potential uses in diverse areas such as materials science, physics, and engineering.

Let us focus on the visual representation of the anisotropic nature of Young's modulus in the materials UP_2, UAs_2, and USb_2, which is depicted in Fig. 6. Anisotropy, in this context, refers to the variation in the value of Young's modulus depending on the direction of measurement. This distinctive characteristic has profound implications on the mechanical behavior of these materials under applied stress.

Young's modulus, symbolized by E, is a measure of the stiffness of a material. It quantifies the relationship between stress (force per unit area) and strain (proportional deformation), thereby defining the material's ability to resist deformation under load. When a material exhibits anisotropy in Young's modulus, it implies that its resistance to deformation is direction-dependent.

For these visualizations, three different sets of conditions were employed. These include PBE-GGA+SP+U (U_{eff} = 0.29 Ry), LDA+SP+U (U_{eff} = 0.15 Ry), and LDA+SP+U (U_{eff} = 0.22 Ry). These conditions, applied to the antiferromagnetic configurations of the materials in question, offer varying perspectives of the anisotropic behavior of Young's modulus.

This anisotropic feature has important implications in the design and potential applications of these materials. For instance, the direction-dependent resistance to deformation could be exploited in engineering and materials science, where materials could be aligned in specific orientations to maximize their resistance to applied forces or optimize their deformability for a given application. Consequently, understanding the anisotropic nature of Young's modulus for these materials forms a crucial component of our broader understanding of their physical and mechanical properties.

As is evident in Fig. 6, the direction-dependence of Young's modulus for the materials UP_2, UAs_2, and USb_2 is illustrated along the (xy), (xz), and (yz) planes. These directional representations, denoted by (a1, b1, c1), (a2, b2, c2), and (a3, b3, c_3) respectively, are critical in elucidating the anisotropic behavior of Young's modulus in these materials.

These figures demonstrate that the Young's modulus for these materials, which essentially measures their ability to resist deformation under applied stress, shows substantial variability depending on the direction of measurement. This variability is a hallmark of the anisotropy of these materials and provides a visual and quantitative reference for understanding the nature of their mechanical responses.

This directional dependence can be interpreted as these materials having distinct stiffness in different directions, which could lead to different mechanical responses when subjected to loads from varying orientations. For example, the material could exhibit higher stiffness (greater resistance to deformation) when a force is applied along the xy plane compared to when the same force is applied along the xz or yz planes. This could be due to various factors such as differences

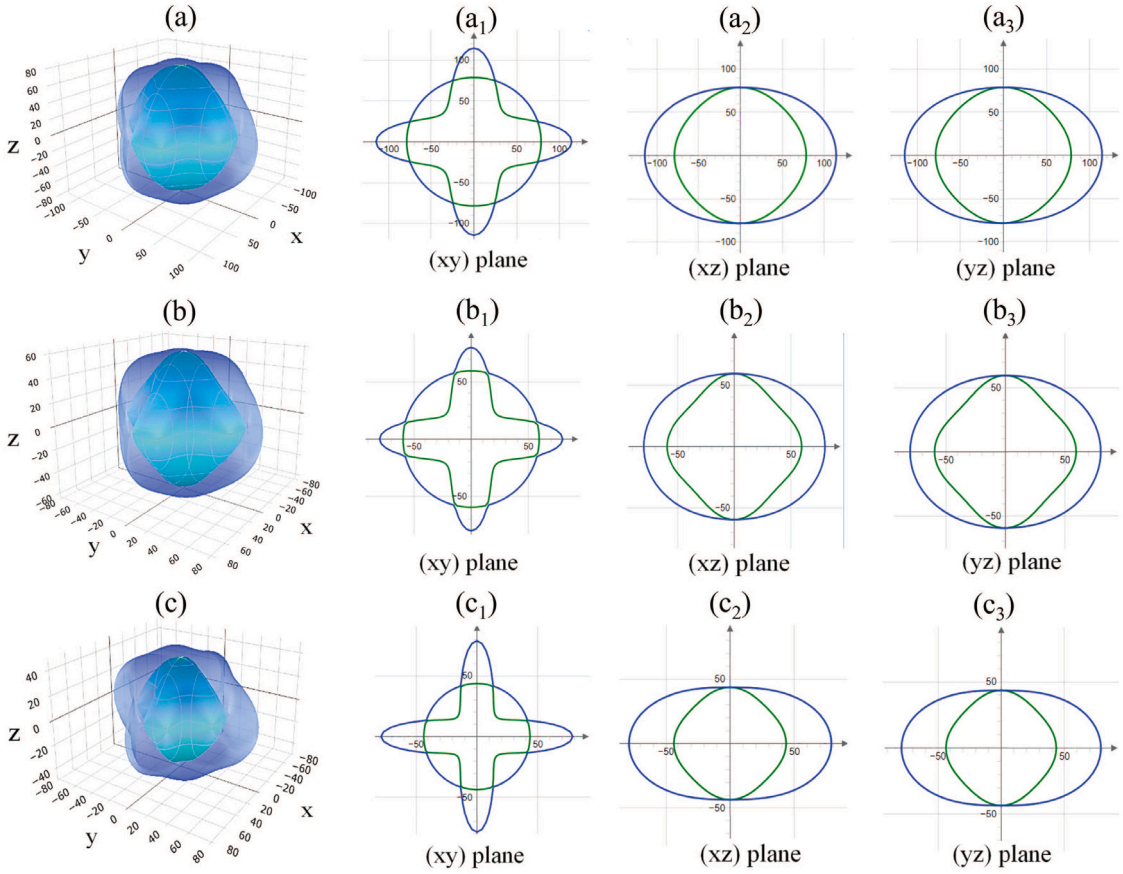

Fig. 7. Spatial dependences of shear moduli calculated by Eq. (63) using the PBE-GGA+SP+U (U_{eff} = 0.29 Ry), LDA+SP+U (U_{eff} = 0.15 Ry), and LDA+SP+U (U_{eff} = 0.22 Ry) for antiferromagnetic (a) UP_2, (b) UAs_2 and (c) USb_2 in their anti-Cu_2Sb-type tetragonal structure and their projections on (a_1), (b_1), and (c_1) (xy) plane, (a_2), (b_2), and (c_2) (xz) plane, and (a_3), (b_3), and c_3 (yz) plane, respectively. SP and U_{eff} represent the spin-polarization and effective Hubbard parameter, respectively.

in bonding strength between atoms, crystallographic arrangements, or other inherent material properties.

Therefore, by visualizing the direction-dependence of Young's modulus in these figures, we gain insights into how these materials might behave under different loading conditions. This is crucial in fields such as materials science and engineering, where materials are often chosen and used based on their mechanical properties, including their anisotropy.

The observation of anisotropy in Young's modulus, as displayed in Fig. 6, is of substantial significance in understanding the inherent properties of the materials UX_2 (where X=P, As, Sb). Young's modulus, as a fundamental property of a material, provides a measure of its resistance to deformation under an applied load—essentially quantifying the material's inherent stiffness. Therefore, the observed anisotropy underscores that the stiffness, and consequently the resistance to deformation, of these materials is not uniformly distributed but rather varies depending on the direction of the applied stress.

Such a finding suggests that the mechanical response of these materials—their deformation and stress–strain relationship—would be dependent on the direction of the applied force. As a consequence, in a practical or experimental setting, these materials could exhibit distinctive mechanical behaviors under different loading conditions, simply based on the direction of the applied load. This anisotropic behavior could result in non-uniform and direction-dependent material response under identical magnitude of stress, a phenomenon that is critical to many material applications.

Furthermore, the anisotropy in Young's modulus can be related to the underlying atomic structures and bonding of these materials. The variation in stiffness might arise due to differences in bonding strength between atoms in different crystallographic planes or directions. This would mean that the atomic arrangement and bonding characteristics in these materials inherently dictate the anisotropic mechanical responses.

Hence, this study does not merely highlight the anisotropic characteristics of UX_2 compounds but provides deeper insights into their structural properties and mechanical behavior, emphasizing the complex and direction-dependent nature of their mechanical responses.

Building upon our understanding of the distinctive mechanical properties of the antiferromagnetic compounds UP_2, UAs_2, and USb_2, we shift our focus to another crucial mechanical property: the shear modulus. The shear modulus provides insight into a material's resistance to shear stress—deformation that occurs when parallel forces are applied in opposite directions. Thus, it offers another perspective on the inherent stiffness of these compounds.

Fig. 7 presents the spatial dependence of the shear modulus, under three different conditions: PBE-GGA+SP+U (U_{eff} = 0.29 Ry), LDA+SP+U (U_{eff} = 0.15 Ry), and LDA+SP+U (U_{eff} = 0.22 Ry). A key observation from these depictions is the clear manifestation of anisotropy in the shear modulus of these compounds. Such an observation is consistent with the anisotropic trends previously noted in linear compressibility and Young's modulus, reaffirming the directional dependence of these materials' mechanical properties.

The directional variation in the shear modulus underpins that these compounds possess different levels of resistance to deformation, specifically to shearing forces, along various crystallographic directions. This again is of profound importance as it indicates how the materials would react to shearing forces, which are prevalent in many real-world applications and scenarios.

The shear modulus anisotropy, when combined with the earlier discussed anisotropic linear compressibility and Young's modulus, reinforces that these antiferromagnetic compounds UP_2, UAs_2, and USb_2

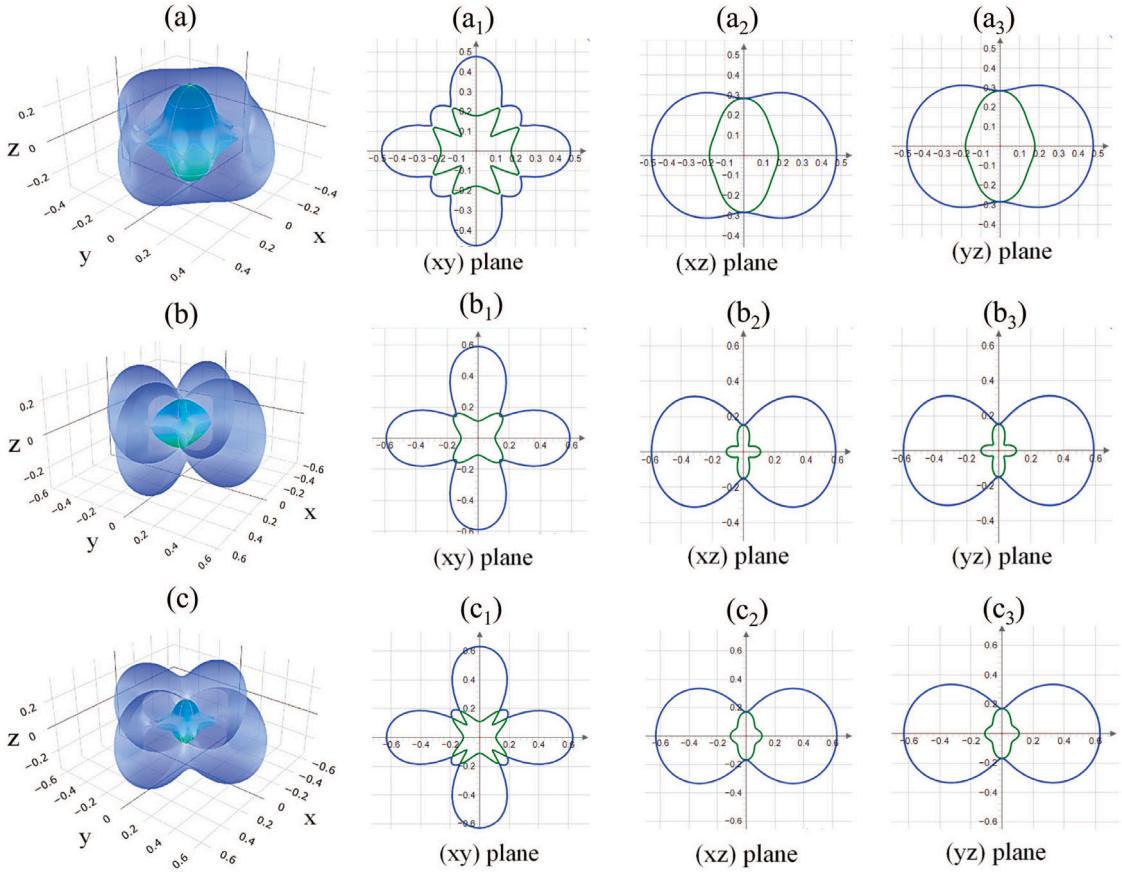

Fig. 8. Spatial dependence of Poisson's ratios calculated by Eq. (64) using the PBE-GGA+SP+U (U_{eff} = 0.29 Ry), LDA+SP+U (U_{eff} = 0.15 Ry), and LDA+SP+U (U_{eff} = 0.22 Ry) for antiferromagnetic (a) UP_2, (b) UAs_2 and (c) USb_2 in their anti-Cu_2Sb-type tetragonal structure and their projections on (a_1), (b_1), and (c_1) (xy) plane, (a_2), (b_2), and (c_2) (xz) plane, and (a_3), (b_3), and c_3 (yz) plane, respectively. SP and U_{eff} represent the spin-polarization and effective Hubbard parameter, respectively.

exhibit mechanical characteristics that significantly vary with direction. This finding reinforces the need for careful consideration of the directional dependence of these properties when proposing these compounds for practical applications. The directionally-dependent resistance to deformation also further hints at the complex interplay of atomic structure and bonding within these materials, resulting in their anisotropic behavior.

Deepening our understanding of the anisotropic shear behavior of the antiferromagnetic compounds UP_2, UAs_2, and USb, we take a further step to analyze the direction-specific representation of the shear modulus. By projecting this key mechanical property along three orthogonal planes—(xy), (xz), and (yz)—we are able to elucidate the precise nature of anisotropy in these materials under shear stress.

In Fig. 7, each compound is mapped individually along these planes. Specifically, subfigures (a1, b1, and c1) illustrate the shear modulus along the (xy) plane, while (a2, b2, and c2) focus on the (xz) plane, and (a3, b3, and c_3) delineate the (yz) plane.

Through these diagrams, we can visualize and gain a comprehensive understanding of the materials' shear resistance across different spatial orientations. For instance, by comparing the shear modulus representations for the (xy), (xz), and (yz) planes, we can discern specific trends or disparities, further evidencing the anisotropic behavior. Such detailed visualizations are vital for understanding how these compounds respond to shear stress in different directions.

By coupling this detailed planar analysis with the broader, global observations from the spatial dependence study, we create a multifaceted understanding of the shear modulus anisotropy in these compounds. This detailed scrutiny provides a broader and more nuanced understanding of the material's mechanical behavior under shear deformation. Understanding these characteristics is essential in practical applications where the materials might be subjected to forces along different axes, thus influencing their behavior and performance.

The shear modulus of the antiferromagnetic compounds UP_2, UAs_2, and USb_2, as depicted in the provided figures, unequivocally demonstrates anisotropic characteristics. This anisotropy reveals that the materials respond differently to shear stress depending on the direction in which the stress is applied. It is this variation in behavior that brings to light the truly complex and intricate nature of the mechanical properties of these compounds.

When speaking of anisotropy in the context of the shear modulus, we are referencing how these materials have direction-dependent mechanical properties. This phenomenon underscores the profound influence of orientation in comprehending and predicting the shear responses of the UX_2 compounds.

Practically, this means that the rigidity of these compounds—their ability to resist shape change under applied shear stress—is not uniform in all directions. For instance, a particular material might exhibit greater resistance to deformation when shear stress is applied along one crystallographic axis compared to another. This orientation-dependent resistance can have significant implications for the application and performance of these materials under real-world conditions where forces may not always be applied uniformly.

Moreover, the observed anisotropy in the shear modulus contributes to our overarching understanding of the complex mechanical behavior of these materials. As such, the anisotropic shear responses of UX_2 compounds should be carefully considered when investigating their potential uses in various applications, particularly in scenarios where they may be subject to different directional forces.

The spatial dependence of Poisson's ratio for the antiferromagnetic compounds UP_2, UAs_2, and USb_2 is depicted in Fig. 8. The examined

Table 9
The minimum and maximum values of linear compressibility (β), Young's modulus (E), shear modulus (G), and Poisson's ratio (ν) considering PBE-GGA+SP+U (U_{eff} = 0.29 Ry), LDA+SP+U (U_{eff} = 0.15 *Ry*), and LDA+SP+U (U_{eff} = 0.22 Ry) respectively for antiferromagnetic UP_2, UAs_2, and USb_2 in their anti-Cu_2Sb-type tetragonal structure. The term "Anisotropy" is used to represent the ratio of the maximum to minimum values of β, E, G, and ν. The term "1st axis" denotes the coordinates (i.e., x, y, or z) at which the maximum and minimum values of β, E, G, and ν are observed. Similarly, "2nd axis" refers to the secondary coordinates where the maximum and minimum values of G and ν are found. The data tabulated here are gleaned from Figs. 5, 6, 7, and 8. The abbreviations SP and U_{eff} correspond to spin-polarization and the effective Hubbard parameter, respectively.

Compound	XCFs	U_{eff} (Ry)		Linear compressibility ($(TPa)^{-1}$)		Young's modulus (GPa)		Shear modulus (GPa)		Poisson's ratio	
				β_{min}	β_{max}	E_{min}	E_{max}	G_{min}	G_{max}	ν_{min}	ν_{max}
UP_2	PBE-GGA+SP+U	0.29	Value	1.818	2.332	148.060	253.220	50.118	114.510	0.106	0.477
			Anisotropy	β_{max}/β_{min} = 1.283		E_{max}/E_{min} = 1.710		G_{max}/G_{min} = 2.285		ν_{max}/ν_{min} = 4.513	
			1st axis	x = 0.0000 y = 0.0000 z = 1.0000	x = 0.8660 y = 0.5000 z = 0.0000	x = 1.0000 y = 0.0000 z = 0.0000	x = 0.7071 y = 0.7071 z = 0.0000	x = −0.7071 y = 0.7071 z = −0.0000	x = 1.0000 y = −0.0002 z = 0.0001	x = 0.7071 y = 0.7071 z = 0.0000	x = 1.0000 y = −0.0000 z = −0.0000
			2nd axis					x = −0.7071 y = −0.7071 z = 0.0000	x = 0.0002 y = 1.0000 z = −0.0000	x = −0.7071 y = 0.7071 z = −0.0000	x = 0.0000 y = 1.0000 z = 0.0000
				β_{min}	β_{max}	E_{min}	E_{max}	G_{min}	G_{max}	ν_{min}	ν_{max}
UAs_2	LDA+SP+U	0.15	Value	3.068	5.117	98.352	191.740	30.946	79.970	0.048	0.589
			Anisotropy	β_{max}/β_{min} = 1.668		E_{max}/E_{min} = 1.950		G_{max}/G_{min} = 2.584		ν_{max}/ν_{min} = 12.333	
			1st axis	x = 0.7934 y = 0.6088 z = 0.0000	x = 0.0000 y = 0.0000 z = 1.0000	x = 1.0000 y = 0.0000 z = 0.0000	x = 0.7071 y = 0.7071 z = 0.0000	x = 0.7071 y = 0.7071 z = 0.0000	x = 1.0000 y = −0.0002 z = 0.0001	x = 0.7242 y = −0.0003 z = 0.6896	x = 1.0000 y = −0.0007 z = 0.0000
			2nd axis					x = −0.7071 y = 0.7071 z = −0.0000	x = 0.0002 y = 1.0000 z = −0.0000	x = 0.6896 y = −0.0006 z = −0.7242	x = 0.0007 y = 1.0000 z = 0.0000
				β_{min}	β_{max}	E_{min}	E_{max}	G_{min}	G_{max}	ν_{min}	ν_{max}
USb_2	LDA+SP+U	0.22	Value	3.484	5.773	74.284	176.680	22.772	78.705	0.086	0.631
			Anisotropy	β_{max}/β_{min} = 1.657		E_{max}/E_{min} = 2.378		G_{max}/G_{min} = 3.456		ν_{max}/ν_{min} = 7.316	
			1st axis	x = 0.7934 y = 0.6088 z = 0.0000	x = 0.0000 y = 0.0000 z = 1.0000	x = 1.0000 y = 0.0000 z = 0.0000	x = 0.7071 y = 0.7071 z = 0.0000	x = −0.7071 y = 0.7071 z = −0.0000	x = 1.0000 y = −0.0002 z = −0.0001	x = 0.7751 y = 0.0001 z = 0.6318	x = 1.0000 y = −0.0002 z = −0.0000
			2nd axis					x = −0.7071 y = −0.7071 z = 0.0000	x = 0.0002 y = 1.0000 z = −0.0000	x = 0.6318 y = 0.0003 z = −0.7751	x = 0.0002 y = 1.0000 z = 0.0000

conditions include the instances of PBE-GGA+SP+U (U_{eff} = 0.29 Ry), LDA+SP+U (U_{eff} = 0.15 Ry), and LDA+SP+U (U_{eff} = 0.22 Ry).

As an essential parameter in material science and engineering, Poisson's ratio provides key insights into how a material deforms under applied stress. Specifically, it quantifies the relationship between longitudinal strain (in the direction of the applied stress) and transverse strain (in the direction perpendicular to the applied stress). In simpler terms, it describes the extent to which a material tends to become thinner in cross-section or expand laterally when stretched longitudinally, and vice versa when compressed.

The spatial distribution of Poisson's ratio, displayed along the (xy), (xz), and (yz) planes, is represented in Fig. 8. We provide a triplet of diagram sets for each compound: (a1, b1, and c1), (a2, b2, and c2), and (a3, b3, and c3), illustrating the Poisson's ratio's behavior in the respective planes.

From these visualizations, it is patently evident that the Poisson's ratio for our subjects of investigation, the UX_2 (X=P, As, Sb) compounds, showcases distinct anisotropic properties. This implies that the materials' response to deformation under stress is not uniform but instead varies with the direction of the applied force. Such directional dependency of deformation responses is a significant factor that could affect their performance in real-world applications.

Finally, to enrich our understanding of these materials, let us conclude our discussion by detailing the range of values for linear compressibility (β), Young's modulus (E), shear modulus (G), and Poisson's ratio (ν) for the UX_2 compounds. As we have extensively discussed, the spatial dependence of these properties is of significant importance. This comprehensive reporting offers crucial insights into the material behavior of the UX_2 compounds. This data can be referenced in Figs. 5, 6, 7, and 8. To simplify the interpretation of this information, we have extracted the minimum and maximum values of these quantities from the latter four figures and summarized them in Table 9. In addition, we have considered the anisotropy in our study. This includes the examination of the extent to which the maximum values exceed the minimum values for β, E, G, and ν. Inspection of the tabulated data reveals clear disparities in the maximum and minimum values of linear compressibility (β), Young's modulus (E), shear modulus (G), and Poisson's ratio (ν) among the UX_2 (X=P, As, Sb) compounds. These variations are indicative not only of the distinct mechanical properties exhibited by each compound but also of their intrinsic anisotropy. To gain a deeper appreciation of the extent of this anisotropy, we have calculated the ratio of maximum to minimum values for each of β, E, G, and ν, which we present as "Anisotropy" in Table 9. This parameter serves as a quantifiable measure of anisotropy, where a ratio of unity implies isotropic behavior, and a ratio deviating from one signifies the presence of anisotropy. We note that the "Anisotropy" values for all UX_2 (X=P, As, Sb) compounds across all parameters exceed one. This unambiguously signals the presence of anisotropy, with the degree of deviation from one providing an indication of the extent of anisotropy. These findings underline the importance of taking into account the direction-dependent mechanical properties of these materials in their application. As the anisotropy can impact the material's response under different mechanical stresses and strains, a comprehensive understanding of these anisotropic characteristics could be crucial in the material's effective usage and could guide the design of future applications. In Table 9, we also provide the axes coordinates (x, y, or z) at which the extreme values of linear compressibility (β), Young's modulus (E), shear modulus (G), and Poisson's ratio (ν) occur. This information gives us insight into the spatial distribution of these properties. The "1st Axis" and "2nd Axis" respectively represent the primary and secondary coordinates where these extremities are observed. This condensed presentation of data serves multiple purposes: it enhances readability, it simplifies the comparison of these properties under different computational methodologies, and it offers an accessible overview of the mechanical behavior of these antiferromagnetic compounds. This table thus acts as an efficient tool for readers to grasp the range and anisotropy of these properties in the studied compounds.

5. Conclusion

This research provides a comprehensive exploration of the elastic and thermal properties of the UX_2 (X=P, As, Sb) compounds. The study affirms their mechanical stability, as evidenced by the calculated elastic constants and their compliance with the Born stability criteria.

We observed a clear trend of declining elastic constants with the substitution of pnictogen atoms from P to As and Sb, accompanied by a concurrent increase in the lattice parameter. Our findings also pointed out a greater susceptibility of these compounds to shear deformation, particularly on the (100) plane, as compared to unidirectional stress along any crystallographic directions.

The study further unraveled intriguing variations within the compounds, with USb_2 manifesting higher compressibility than UP_2 and UAs_2. Moreover, it identified enhanced elasticity along the (001) plane, relative to the *c*-axis bonding. Strikingly, all compounds examined displayed a close proximity to the brittle/ductile borderline, when gauged using Pugh's ratio and Poisson's ratio.

In the realm of thermal properties, UP_2 stood out with its superior Debye temperature, signaling its potential for high-temperature applications. Additionally, our calculations of high melting temperatures for these compounds aligned well with the estimated heat capacities and existing experimental data, hinting at the practical utility of these materials.

These compelling thermal properties of the UX_2 compounds suggest promising applications across sectors such as energy production, manufacturing, and materials science. The resilience of these materials under high-temperature conditions positions them as strong contenders in industries and research areas that require substantial thermal resistance.

One of the salient aspects of our investigation was the uncovering of the link between the lattice parameter variation and the melting temperature as we transition from P to As, and then from As to Sb within the UX_2 compounds. This relation underscores how the microscopic alterations in atomic structure can significantly influence the macroscopic thermal properties of a material. Such a comprehension could guide the design of future materials, facilitating the synthesis of compounds with desired thermal properties by manipulating structural parameters at the microscale level.

However, we recognize that our findings form part of a complex picture, with a myriad of other factors potentially contributing to the observed thermal trends. Further theoretical and experimental work is needed to fully understand the interplay between these different factors, such as structural parameters, electronic configurations, and bonding characteristics, and how they collectively influence the thermal properties of these compounds.

Despite this complexity, our study provides a significant stepping-stone for future research. The key findings, namely the atomic constitution's impact on anisotropic heat conduction and the consistently higher minimum thermal conductivity along specific crystallographic orientations, present compelling implications for real-world applications, especially those demanding superior thermal management. These insights bridge the gap between theoretical understanding and practical application, fostering the possibility of advancements in new technologies and materials science.

Further anisotropy calculations and wave velocity assessments emphasize the faster propagation of longitudinal waves than transverse ones, contributing to our understanding of these compounds' anisotropic behavior. Notably, the highest anisotropy in both shear and compression was exhibited by UP_2, underscoring the diverse behavior of these compounds under different conditions.

To conclude, this study significantly enhances our understanding of the antiferromagnetic UX_2 (X=P, As, Sb) compounds' mechanical and thermal properties. The unique insights into the patterns of shear deformation, compressibility, and thermal characteristics could serve as a guide for their prospective applications, particularly in high-temperature environments. The knowledge acquired forms a crucial pillar for future technological developments, holding the potential to revolutionize the synthesis and application of materials in the future.

CRediT authorship contribution statement

Reyhaneh Ebrahimi-Jaberi: Conceptualization, Data curation, Formal analysis, Investigation, Methodology, Validation, Visualization, Writing – original draft. **S. Jalali-Asadabadi:** Conceptualization, Data curation, Formal analysis, Funding acquisition, Investigation, Methodology, Project administration, Resources, Software, Supervision, Validation, Visualization, Writing – original draft, Writing – review & editing.

Declaration of competing interest

The authors declare that they have no known competing financial interests or personal relationships that could have appeared to influence the work reported in this paper.

Data availability

Data will be made available on request.

Acknowledgments

This work forms a part of the doctoral research undertaken by Reyhaneh Ebrahimi-Jaberi, under the expert supervision of Dr. S. Jalali-Asadabadi. We would like to express our sincere gratitude to the University of Isfahan (UI) for their invaluable support and contributions to this study.

References

[1] T.T.M. Palstra, A.A. Menovsky, J. van den Berg, A.J. Dirkmaat, P.H. Kes, G.J. Nieuwenhuys, J.A. Mydosh, Superconducting and magnetic transitions in the heavy-Fermion system URu_2Si_2, Phys. Rev. Lett. 55 (1985) 2727–2730, http://dx.doi.org/10.1103/PhysRevLett.55.2727, URL https://link.aps.org/doi/10.1103/PhysRevLett.55.2727.

[2] M.B. Maple, J.W. Chen, Y. Dalichaouch, T. Kohara, C. Rossel, M.S. Torikachvili, M.W. McElfresh, J.D. Thompson, Partially gapped Fermi surface in the heavy-electron superconductor URu_2Si_2, Phys. Rev. Lett. 56 (1986) 185–188, http://dx.doi.org/10.1103/PhysRevLett.56.185, URL https://link.aps.org/doi/10.1103/PhysRevLett.56.185.

[3] R. Fisher, S. Kim, Y. Wu, N. Phillips, M. McElfresh, M. Torikachvili, M. Maple, Specific heat of URu_2Si_2: Effect of pressure and magnetic field on the magnetic and superconducting transitions, Physica B 163 (1) (1990) 419–423, http://dx.doi.org/10.1016/0921-4526(90)90229-N, URL https://www.sciencedirect.com/science/article/pii/092145269090229N.

[4] C. Pfleiderer, Superconducting phases of f-electron compounds, Rev. Modern Phys. 81 (2009) 1551–1624, http://dx.doi.org/10.1103/RevModPhys.81.1551, URL https://link.aps.org/doi/10.1103/RevModPhys.81.1551.

[5] K.T. Moore, G. van der Laan, Nature of the $5f$ states in actinide metals, Rev. Modern Phys. 81 (2009) 235–298, http://dx.doi.org/10.1103/RevModPhys.81.235, URL https://link.aps.org/doi/10.1103/RevModPhys.81.235.

[6] J. Leciejewicz, R. Troć, A. Murasik, A. Zygmunt, Neutron-diffraction study of antiferromagnetism in USb_2 and UBi_2, Phys. Status Solidi (B) 22 (2) (1967) 517–526, http://dx.doi.org/10.1002/pssb.19670220224, URL https://onlinelibrary.wiley.com/doi/abs/10.1002/pssb.19670220224.

[7] J. Qi, T. Durakiewicz, S.A. Trugman, J.-X. Zhu, P.S. Riseborough, R. Baumbach, E.D. Bauer, K. Gofryk, J.-Q. Meng, J.J. Joyce, A.J. Taylor, R.P. Prasankumar, Measurement of two low-temperature energy gaps in the electronic structure of antiferromagnetic USb_2 using ultrafast optical spectroscopy, Phys. Rev. Lett. 111 (2013) 057402, http://dx.doi.org/10.1103/PhysRevLett.111.057402, URL https://link.aps.org/doi/10.1103/PhysRevLett.111.057402.

[8] D.H. Xie, M.L. Li, W. Zhang, L. Huang, W. Feng, Y. Fang, Y. Zhang, Q.Y. Chen, X.G. Zhu, Q. Liu, B.K. Yuan, L.Z. Luo, P. Zhang, X.C. Lai, S.Y. Tan, Direct measurement of the localized-itinerant transition, hybridization and antiferromagnetic transition of 5f electrons, 2017.

[9] R.L. Stillwell, I.-L. Liu, N. Harrison, M. Jaime, J.R. Jeffries, N.P. Butch, Tricritical point of the f-electron antiferromagnet USb_2 driven by high magnetic fields, Phys. Rev. B 95 (2017) 014414, http://dx.doi.org/10.1103/PhysRevB.95.014414, URL https://link.aps.org/doi/10.1103/PhysRevB.95.014414.

[10] J.R. Jeffries, R.L. Stillwell, S.T. Weir, Y.K. Vohra, N.P. Butch, Emergent ferromagnetism and T-linear scattering in USb_2 at high pressure, Phys. Rev. B 93 (2016) 184406, http://dx.doi.org/10.1103/PhysRevB.93.184406, URL https://link.aps.org/doi/10.1103/PhysRevB.93.184406.

[11] L. Miao, R. Basak, S. Ran, Y. Xu, E. Kotta, H. He, J.D. Denlinger, Y.-D. Chuang, Y. Zhao, Z. Xu, et al., High temperature singlet-based magnetism from Hund's rule correlations, Nat. Commun. 10 (1) (2019) 1–8.

[12] E. Ghasemikhah, S. Jalali Asadabadi, I. Ahmad, M. Yazdani-Kacoei, Ab initio studies of electric field gradients and magnetic properties of uranium dipnicties, RSC Adv. 5 (2015) 37592–37602, http://dx.doi.org/10.1039/C5RA02881G.

[13] M. Zarshenas, S. Jalali Asadabadi, Theoretical study of α-U/W(110) thin films from density functional theory calculations: Structural, magnetic and electronic properties, Thin Solid Films 520 (7) (2012) 2901–2908, http://dx.doi.org/10.1016/j.tsf.2011.12.040, URL https://www.sciencedirect.com/science/article/pii/S0040609011021420.

[14] S. Lebègue, P.M. Oppeneer, O. Eriksson, Ab initio study of the electronic properties and Fermi surface of the uranium dipnictides, Phys. Rev. B 73 (2006) 045119, http://dx.doi.org/10.1103/PhysRevB.73.045119, URL https://link.aps.org/doi/10.1103/PhysRevB.73.045119.

[15] D. Aoki, P. Wiśniewski, K. Miyake, N. Watanabe, Y. Inada, R. Settai, E. Yamamoto, Y. Haga, Y. Onuki, Cylindrical Fermi surfaces formed by a fiat magnetic Brillouin zone in uranium dipnictides, Philos. Mag. B 80 (8) (2000) 1517–1544, http://dx.doi.org/10.1080/13642810008208582.

[16] D. Aoki, P. Wiśniewski, K. Miyake, N. Watanabe, Y. Inada, R. Settai, E. Yamamoto, Y. Haga, Y. Onuki, Crystal growth and cylindrical Fermi surfaces of USb_2, J. Phys. Soc. Japan 68 (7) (1999) 2182–2185.

[17] E. Guziewicz, T. Durakiewicz, M.T. Butterfield, C.G. Olson, J.J. Joyce, A.J. Arko, J.L. Sarrao, D.P. Moore, L. Morales, Angle-resolved photoemission study of USb_2 : The $5f$ band structure, Phys. Rev. B 69 (2004) 045102, http://dx.doi.org/10.1103/PhysRevB.69.045102, URL https://link.aps.org/doi/10.1103/PhysRevB.69.045102.

[18] S. Tsutsui, M. Nakada, S. Nasu, Y. Haga, D. Aoki, P. Wiśniewski, Y. Ōnuki, Y., Hyperfine interactions in the antiferromagnetic states of UX_2 (X=P,As,Sb,Bi), Phys. Rev. B 69 (2004) 054404, http://dx.doi.org/10.1103/PhysRevB.69.054404, URL https://link.aps.org/doi/10.1103/PhysRevB.69.054404.

[19] F. Friedman, J. Grunzweig, M. Kuznietz, Knigth shift of 31P NMR in the paramagnetic state of uranium phosphides, Phys. Lett. A 25 (9) (1967) 690–692, http://dx.doi.org/10.1016/0375-9601(67)90477-X, URL https://www.sciencedirect.com/science/article/pii/037596016790477X.

[20] M.M. Wysokiński, Microscopic mechanism for the unusual antiferromagnetic order and the pressure-induced transition to ferromagnetism in USb_2, Phys. Rev. B 97 (2018) http://dx.doi.org/10.1103/PhysRevB.97.041107, 041107(R). URL https://link.aps.org/doi/10.1103/PhysRevB.97.041107.

[21] G. Amoretti, A. Blaise, J. Mulak, Crystal field interpretation of the magnetic properties of UX_2 compounds (X=P, As, Sb, Bi), J. Magn. Magn. Mater. 42 (1) (1984) 65–72, http://dx.doi.org/10.1016/0304-8853(84)90291-9, URL https://www.sciencedirect.com/science/article/pii/0304885384902919.

[22] K. Easwaran, V.S. Rao, R. Vijayaraghavan, U. Rao, Nuclear magnetic resonance of 31P in the paramagnetic state of UP_2, Phys. Lett. A 25 (9) (1967) 683–684, http://dx.doi.org/10.1016/0375-9601(67)90473-2, URL https://www.sciencedirect.com/science/article/pii/0375960167904732.

[23] Z. Henkie, R. Maślanka, P. Wiśniewski, R. Fabrowski, P. Markowski, J. Franse, M. van Sprang, Anisotropy of the physical properties of uniaxial antiferromagnetic USb_2, J. Alloys Compd. 181 (1) (1992) 267–273, http://dx.doi.org/10.1016/0925-8388(92)90321-Y, URL https://www.sciencedirect.com/science/article/pii/092583889290321Y. Proceedings of the 19th Rare Earth Research Conference.

[24] Z. Henkie, P. Markowski, Crystal growth of uranium and thorium compounds with the elements of group V by chemical vapor transport, J. Cryst. Growth 41 (2) (1977) 303–308, http://dx.doi.org/10.1016/0022-0248(77)90059-8, URL https://www.sciencedirect.com/science/article/pii/0022024877900598.

[25] Z. Henkie, W. Trzebiatowski, Electrical properties of monocrystalline uranium diphosphide, Phys. Status Solidi (B) 35 (2) (1969) 827–834, http://dx.doi.org/10.1002/pssb.19690350232, URL https://onlinelibrary.wiley.com/doi/abs/10.1002/pssb.19690350232.

[26] Z. Henkie, P. Wiśniewski, R. Fabrowski, R. Maślanka, Dependence of ordering temperature on pressure, carrier density and U-U distance in uranium pnictides; pressure and hall effects examinations of UP_2 and USb_2, Solid State Commun. 79 (12) (1991) 1025–1028, http://dx.doi.org/10.1016/0038-1098(91)90002-D, URL https://www.sciencedirect.com/science/article/pii/003810989190002D.

[27] F. Grønvold, M.R. Zaki, E.F. Westrum, J.A. Sommers, D.B. Downie, Actinoid pnictides—II: Heat capacities of UAs_2 and USb_2 from 5 to 750 K and antiferromagnetic transitions, J. Inorg. Nucl. Chem. 40 (4) (1978) 635–645, http://dx.doi.org/10.1016/0022-1902(78)80379-0, URL https://www.sciencedirect.com/science/article/pii/0022190278803790.

[28] P. Wiśniewski, D. Aoki, K. Miyake, N. Watanabe, Y. Inada, R. Settai, Y. Haga, E. Yamamoto, Y. Ōnuki, Cylindrical Fermi surfaces of UAs_2 and UP_2, Physica B 281–282 (2000) 769–770, http://dx.doi.org/10.1016/S0921-4526(99)00918-7, URL https://www.sciencedirect.com/science/article/pii/S0921452699009187.

[29] P. Wiśniewski, D. Aoki, N. Watanabe, R. Settai, Y. Haga, E. Yamamoto, Y. Ōnuki, Shubnikov–de Haas effect study of cylindrical Fermi surfaces in UP_2, J. Phys. Soc. Japan 70 (1) (2001) 278–283, http://dx.doi.org/10.1143/JPSJ.70.278.

[30] P. Wiśniewski, D. Aoki, N. Watanabe, K. Miyake, R. Settai, Y. Ōnuki, Y. Haga, E. Yamamoto, Z. Henkie, Shubnikov-de Haas effect study of cylindrical Fermi surfaces in UAs_2, J. Phys.: Condens. Matter 12 (9) (2000) 1971–1980, http://dx.doi.org/10.1088/0953-8984/12/9/302.

[31] R. Wawryk, Magnetic and transport properties of UBi_2 and USb_2 single crystals, Phil. Mag. 86 (12) (2006) 1775–1787, http://dx.doi.org/10.1080/14786430500501663.

[32] H. Adachi, S. Imoto, Magnetic susceptibility and electrical resistivity of uranium phosphides and UP-ThP solid solutions, J. Nucl. Sci. Technol. 6 (9) (1969) 531–535, http://dx.doi.org/10.1080/18811248.1969.9732939, URL https://www.tandfonline.com/doi/abs/10.1080/18811248.1969.9732939.

[33] S. Chen, M. Hawley, P.V. Stockum, H. Manoharan, E. Bauer, Surface structure of cleaved (001) USb_2 single crystal, Phil. Mag. 89 (22–24) (2009) 1881–1891, http://dx.doi.org/10.1080/14786430902785336.

[34] R. Wawryk, J. Mucha, H. Misiorek, Z. Henkie, Thermal conductivity of USb_2 and UBi_2 single crystals, Phil. Mag. 90 (6) (2010) 793–801, http://dx.doi.org/10.1080/14786430903292399.

[35] K. Choudhary, G. Cheon, E. Reed, F. Tavazza, Elastic properties of bulk and low-dimensional materials using van der Waals density functional, Phys. Rev. B 98 (2018) 014107, http://dx.doi.org/10.1103/PhysRevB.98.014107, URL https://link.aps.org/doi/10.1103/PhysRevB.98.014107.

[36] S. Singh, I. Valencia-Jaime, O. Pavlic, A.H. Romero, Elastic, mechanical, and thermodynamic properties of Bi-Sb binaries: Effect of spin-orbit coupling, Phys. Rev. B 97 (2018) 054108, http://dx.doi.org/10.1103/PhysRevB.97.054108, URL https://link.aps.org/doi/10.1103/PhysRevB.97.054108.

[37] R.J. Schiltz, J.F. Smith, Elastic constants of some MAl_2 single crystals, J. Appl. Phys. 45 (11) (1974) 4681–4685, http://dx.doi.org/10.1063/1.1663118.

[38] M. Sanati, R.C. Albers, T. Lookman, A. Saxena, Elastic constants, phonon density of states, and thermal properties of UO_2, Phys. Rev. B 84 (2011) 014116, http://dx.doi.org/10.1103/PhysRevB.84.014116, URL https://link.aps.org/doi/10.1103/PhysRevB.84.014116.

[39] M. Shafiq, S. Arif, I. Ahmad, S.J. Asadabadi, M. Maqbool, H. Rahnamaye Aliabad, Elastic and mechanical properties of lanthanide monoxides, J. Alloys Compd. 618 (2015) 292–298, http://dx.doi.org/10.1016/j.jallcom.2014.08.171, URL https://www.sciencedirect.com/science/article/pii/S0925838814020374.

[40] X. Zeng, R. Peng, Y. Yu, Z. Hu, Y. Wen, L. Song, Pressure effect on elastic constants and related properties of Ti_3Al intermetallic compound: A first-principles study, Materials 11 (10) (2018) http://dx.doi.org/10.3390/ma11102015, URL https://www.mdpi.com/1996-1944/11/10/2015.

[41] Y. Wen, L. Wang, H. Liu, L. Song, Ab initio study of the elastic and mechanical properties of B19 TiAl, Crystals 7 (2) (2017) http://dx.doi.org/10.3390/cryst7020039, URL https://www.mdpi.com/2073-4352/7/2/39.

[42] S.L. Shang, Y. Wang, D.E. Kim, C.L. Zacherl, Y. Du, Z.K. Liu, Structural, vibrational, and thermodynamic properties of ordered and disordered $Ni_{1-x}Pt_x$ alloys from first-principles calculations, Phys. Rev. B 83 (2011) 144204, http://dx.doi.org/10.1103/PhysRevB.83.144204, URL https://link.aps.org/doi/10.1103/PhysRevB.83.144204.

[43] M. Jamal, M. Bilal, I. Ahmad, S. Jalali-Asadabadi, IRelast package, J. Alloys Compd. 735 (2018) 569–579, http://dx.doi.org/10.1016/j.jallcom.2017.10.139, URL https://www.sciencedirect.com/science/article/pii/S0925838817335752.

[44] M. Jamal, S. Jalali Asadabadi, I. Ahmad, H. Rahnamaye Aliabad, Elastic constants of cubic crystals, Comput. Mater. Sci. 95 (2014) 592–599, http://dx.doi.org/10.1016/j.commatsci.2014.08.027, URL http://www.sciencedirect.com/science/article/pii/S0927025614005692.

[45] P. Blaha, K. Schwarz, F. Tran, R. Laskowski, G.K.H. Madsen, L.D. Marks, WIEN2k: An APW+lo program for calculating the properties of solids, J. Chem. Phys. 152 (7) (2020) 074101, http://dx.doi.org/10.1063/1.5143061.

[46] J.P. Perdew, Y. Wang, Accurate and simple analytic representation of the electron-gas correlation energy, Phys. Rev. B 45 (1992) 13244–13249, http://dx.doi.org/10.1103/PhysRevB.45.13244, URL https://link.aps.org/doi/10.1103/PhysRevB.45.13244.

[47] J.P. Perdew, K. Burke, M. Ernzerhof, Generalized gradient approximation made simple, Phys. Rev. Lett. 77 (1996) 3865–3868, http://dx.doi.org/10.1103/PhysRevLett.77.3865, URL https://link.aps.org/doi/10.1103/PhysRevLett.77.3865.

[48] J. Yu, A.J. Freeman, R. Podloucky, P. Herzig, P. Weinberger, Origin of electric-field gradients in high-temperature superconductors: $YBa_2Cu_3O_7$, Phys. Rev. B 43 (1991) 532–541, http://dx.doi.org/10.1103/PhysRevB.43.532, URL https://link.aps.org/doi/10.1103/PhysRevB.43.532.

[49] K. Schwarz, C. Ambrosch-Draxl, P. Blaha, Charge distribution and electric-field gradients in $YBa_2Cu_3O_{7-x}$, Phys. Rev. B 42 (1990) 2051–2061, http://dx.doi.org/10.1103/PhysRevB.42.2051, URL https://link.aps.org/doi/10.1103/PhysRevB.42.2051.

[50] S. Jalali Asadabadi, Electronic structure and electric-field gradient analysis in $CeIn_3$, Phys. Rev. B 75 (2007) 205130, http://dx.doi.org/10.1103/PhysRevB.75.205130, URL https://link.aps.org/doi/10.1103/PhysRevB.75.205130.

[51] S.J. Asadabadi, S. Cottenier, H. Akbarzadeh, R. Saki, M. Rots, Valency of rare earths in RIn_3 and RSn_3 : Ab initio analysis of electric-field gradients, Phys. Rev. B 66 (2002) 195103, http://dx.doi.org/10.1103/PhysRevB.66.195103, URL https://link.aps.org/doi/10.1103/PhysRevB.66.195103.

[52] S. Jalali Asadabadi, H. Akbarzadeh, Density functional approach to study structural properties and electric field gradients in rare earth materials, Physica B 349 (1) (2004) 76–83, http://dx.doi.org/10.1016/j.physb.2004.01.153, URL https://www.sciencedirect.com/science/article/pii/S0921452604001930.

[53] M. Yazdani-Kachoei, S. Jalali-Asadabadi, I. Ahmad, K. Zarringhalam, Pressure dependency of localization degree in heavy fermion CeIn3: A density functional theory analysis, Sci. Rep. 6 (1) (2016) 31734, http://dx.doi.org/10.1038/srep31734.

[54] M. Rafiee, S. Jalali Asadabadi, Quantum size effects in Pb/Si(111) thin films from density functional calculations, Comput. Mater. Sci. 47 (2) (2009) 584–592, http://dx.doi.org/10.1016/j.commatsci.2009.09.027, URL https://www.sciencedirect.com/science/article/pii/S0927025609003711.

[55] A.D. Becke, Perspective: Fifty years of density-functional theory in chemical physics, J. Chem. Phys. 140 (18) (2014) 18A301, http://dx.doi.org/10.1063/1.4869598.

[56] R. Yu, X.F. Zhang, L.C. De Jonghe, R.O. Ritchie, Elastic constants and tensile properties of Al_2OC by density functional calculations, Phys. Rev. B 75 (2007) 104114, http://dx.doi.org/10.1103/PhysRevB.75.104114, URL https://link.aps.org/doi/10.1103/PhysRevB.75.104114.

[57] S.P. Łepkowski, I. Gorczyca, Ab initio study of elastic constants in $In_xGa_{1-x}N$ and $In_xAl_{1-x}N$ wurtzite alloys, Phys. Rev. B 83 (2011) 203201, http://dx.doi.org/10.1103/PhysRevB.83.203201, URL https://link.aps.org/doi/10.1103/PhysRevB.83.203201.

[58] M.-Y. Xie, F. Tasnádi, I.A. Abrikosov, L. Hultman, V. Darakchieva, Elastic constants, composition, and piezoelectric polarization in $In_xAl_{1-x}N$: From ab initio calculations to experimental implications for the applicability of Vegard's rule, Phys. Rev. B 86 (2012) 155310, http://dx.doi.org/10.1103/PhysRevB.86.155310, URL https://link.aps.org/doi/10.1103/PhysRevB.86.155310.

[59] M. Shafiq, I. Ahmad, S. Jalali Asadabadi, Theoretical studies of strongly correlated rare-earth intermetallics $RIn_3 and RSn_3$(R=Sm, Eu, and Gd), J. Appl. Phys. 116 (10) (2014) 103905, http://dx.doi.org/10.1063/1.4894833.

[60] S. Ahmad, R. Ahmad, S. Jalali-Asadabadi, Z. Ali, I. Ahmad, First principle studies of structural, magnetic and elastic properties of orthorhombic rare-earth diaurides intermetallics RAu2 (R=La, Ce, Pr and Eu), Mater. Chem. Phys. 212 (2018) 44–50, http://dx.doi.org/10.1016/j.matchemphys.2018.03.028, URL https://www.sciencedirect.com/science/article/pii/S0254058418301913.

[61] R. Ebrahimi-Jaberi;, J. Nematollahi, H. Gharagoozloo, S. Jalali-Asadabadi, M. Jamal, Elastic constants and their variation by pressure in the cubic $PbTiO_3$ compound using IRelast computational package within the density functional theory, Iranian J. Phys. Res. 19 (1) (2019) 37–48, http://dx.doi.org/10.29252/ijpr.19.1.5.

[62] R. Iqbal, M. Bilal, S. Jalali-Asadabadi, H.A. Rahnamaye Aliabad, I. Ahmad, Theoretical investigation of thermoelectric and elastic properties of intermetallic compounds ScTM (TM=Cu, Ag, Au and Pd), Internat. J. Modern Phys. B 32 (02) (2018) 1850004, http://dx.doi.org/10.1142/S0217979218500042.

[63] M. Shafiq, I. Khan, I. Ahmad, Z. Ali, S. Jalali-Asadabadi, I. Ahmad, A. Laref, Y. Saeed, Structural, elastic and thermal properties of lanthanide monoantimonides, J. Appl. Mater. Sci. Eng. Res. 2 (2019) 1–10, http://dx.doi.org/10.33140/amse/02/01/29.

[64] J. Callaway, Quantum Theory of the Solid State, Academic Press, 2013.

[65] G. Mase, G. Mase, Elasticity: Theory, Applications, and Numerics, CRC Press LLC, New York, 1999.

[66] P. Brüesch, Phonons: Theory and Experiments I: Lattice Dynamics and Models of Interatomic Forces. Vol. 34, Springer Science & Business Media, 2012.

[67] H. Yao, L. Ouyang, W.-Y. Ching, Ab initio calculation of elastic constants of ceramic crystals, J. Am. Ceram. Soc. 90 (10) (2007) 3194–3204, http://dx.doi.org/10.1111/j.1551-2916.2007.01931.x, URL https://ceramics.onlinelibrary.wiley.com/doi/abs/10.1111/j.1551-2916.2007.01931.x.

[68] Y. He, V. Cvetkovic, C.M. Varma, Elastic properties of a class of solids with negative thermal expansion, Phys. Rev. B 82 (2010) 014111, http://dx.doi.org/10.1103/PhysRevB.82.014111, URL https://link.aps.org/doi/10.1103/PhysRevB.82.014111.

[69] A.E. Petrova, V.N. Krasnorussky, A.A. Shikov, W.M. Yuhasz, T.A. Lograsso, J.C. Lashley, S.M. Stishov, Elastic, thermodynamic, and electronic properties of MnSi, FeSi, and CoSi, Phys. Rev. B 82 (2010) 155124, http://dx.doi.org/10.1103/PhysRevB.82.155124, URL https://link.aps.org/doi/10.1103/PhysRevB.82.155124.

[70] V. Kanchana, G. Vaitheeswaran, X. Zhang, Y. Ma, A. Svane, O. Eriksson, Lattice dynamics and elastic properties of the $4f$ electron system: CeN, Phys. Rev. B 84 (2011) 205135, http://dx.doi.org/10.1103/PhysRevB.84.205135, URL https://link.aps.org/doi/10.1103/PhysRevB.84.205135.

[71] W.B. Daniels, Pressure variation of the elastic constants of sodium, Phys. Rev. J. Arch. 119 (1960) 1246–1252, http://dx.doi.org/10.1103/PhysRev.119.1246, URL https://link.aps.org/doi/10.1103/PhysRev.119.1246.

[72] R. Stadler, W. Wolf, R. Podloucky, G. Kresse, J. Furthmüller, J. Hafner, Ab initio calculations of the cohesive, elastic, and dynamical properties of $CoSi_2$ by pseudopotential and all-electron techniques, Phys. Rev. B 54 (1996) 1729–1734, http://dx.doi.org/10.1103/PhysRevB.54.1729, URL https://link.aps.org/doi/10.1103/PhysRevB.54.1729.

[73] B. Wen, T. Shao, R. Melnik, Y. Kawazoe, Y. Tian, Temperature and pressure dependent geometry optimization and elastic constant calculations for arbitrary symmetry crystals: Applications to $MgSiO_3$ perovskites, J. Appl. Phys. 113 (10) (2013) 103501, http://dx.doi.org/10.1063/1.4794360.

[74] O.H. Nielsen, R.M. Martin, First-principles calculation of stress, Phys. Rev. Lett. 50 (1983) 697–700, http://dx.doi.org/10.1103/PhysRevLett.50.697, URL https://link.aps.org/doi/10.1103/PhysRevLett.50.697.

[75] J. Dellinger, D. Vasicek, C. Sondergeld, Kelvin notation for stabilizing elastic-constant inversion, Revue De L'institut Français Du Pétrole 53 (5) (1998) 709–719, http://dx.doi.org/10.2516/ogst:1998063.

[76] J.F. Nye, et al., Physical Properties of Crystals: Their Representation By Tensors and Matrices, Oxford University Press, 1985.

[77] A. Reshak, M. Jamal, DFT calculation for elastic constants of tetragonal structure of crystalline solids with WIEN2k code: A new package (Tetra-elastic), Int. J. Electrochem. Sci. 8 (2013) 12252–12263.

[78] P. Hohenberg, W. Kohn, Inhomogeneous electron gas, Phys. Rev. J. Arch. 136 (1964) B864–B871, http://dx.doi.org/10.1103/PhysRev.136.B864, URL https://link.aps.org/doi/10.1103/PhysRev.136.B864.

[79] W. Kohn, L.J. Sham, Self-consistent equations including exchange and correlation effects, Phys. Rev. J. Arch. 140 (1965) A1133–A1138, http://dx.doi.org/10.1103/PhysRev.140.A1133, URL https://link.aps.org/doi/10.1103/PhysRev.140.A1133.

[80] P. Blaha, K. Schwarz, P. Sorantin, S. Trickey, Full-potential, linearized augmented plane wave programs for crystalline systems, Comput. Phys. Comm. 59 (2) (1990) 399–415, http://dx.doi.org/10.1016/0010-4655(90)90187-6, URL https://www.sciencedirect.com/science/article/pii/0010465590901876.

[81] G.K.H. Madsen, P. Blaha, K. Schwarz, E. Sjöstedt, L. Nordström, Efficient linearization of the augmented plane-wave method, Phys. Rev. B 64 (2001) 195134, http://dx.doi.org/10.1103/PhysRevB.64.195134, URL https://link.aps.org/doi/10.1103/PhysRevB.64.195134.

[82] R. Gaillac, P. Pullumbi, F.-X. Coudert, ELATE: An open-source online application for analysis and visualization of elastic tensors, J. Phys.: Condens. Matter 28 (27) (2016) 275201, http://dx.doi.org/10.1088/0953-8984/28/27/275201.

[83] H.J. Monkhorst, J.D. Pack, Special points for Brillouin-zone integrations, Phys. Rev. B 13 (1976) 5188–5192, http://dx.doi.org/10.1103/PhysRevB.13.5188, URL https://link.aps.org/doi/10.1103/PhysRevB.13.5188.

[84] P. Blaha, K. Schwarz, G.K. Madsen, D. Kvasnicka, J. Luitz, et al., wien2k, in: An Augmented Plane Wave+ Local Orbitals Program for Calculating Crystal Properties. Vol. 60, 2001.

[85] A. Östlin, L. Vitos, L. Chioncel, Analytic continuation-free Green's function approach to correlated electronic structure calculations, Phys. Rev. B 96 (2017) 125156, http://dx.doi.org/10.1103/PhysRevB.96.125156, URL https://link.aps.org/doi/10.1103/PhysRevB.96.125156.

[86] V.I. Anisimov, J. Zaanen, O.K. Andersen, Band theory and Mott insulators: Hubbard U instead of Stoner I, Phys. Rev. B 44 (1991) 943–954, http://dx.doi.org/10.1103/PhysRevB.44.943, URL https://link.aps.org/doi/10.1103/PhysRevB.44.943.

[87] V.I. Anisimov, I.V. Solovyev, M.A. Korotin, M.T. Czyżyk, G.A. Sawatzky, Density-functional theory and NiO photoemission spectra, Phys. Rev. B 48 (1993) 16929–16934, http://dx.doi.org/10.1103/PhysRevB.48.16929, URL https://link.aps.org/doi/10.1103/PhysRevB.48.16929.

[88] M.T. Czyżyk, G.A. Sawatzky, Local-density functional and on-site correlations: The electronic structure of La_2CuO_4 and $LaCuO_3$, Phys. Rev. B 49 (1994) 14211–14228, http://dx.doi.org/10.1103/PhysRevB.49.14211, URL https://link.aps.org/doi/10.1103/PhysRevB.49.14211.

[89] V.I. Anisimov, F. Aryasetiawan, A.I. Lichtenstein, First-principles calculations of the electronic structure and spectra of strongly correlated systems: the LDA + U method, J. Phys.: Condens. Matter 9 (4) (1997) 767–808, http://dx.doi.org/10.1088/0953-8984/9/4/002.

[90] A. Togo, F. Oba, I. Tanaka, First-principles calculations of the ferroelastic transition between rutile-type and CaCl2- type SiO2 at high pressures, Phys. Rev. B 78 (13) (2008) 134106.

[91] P. Brüesch, Phonons: Theory and Experiments I: Lattice Dynamics and Modelsof Interatomic Forces, first ed., Springer-Verlag, Berlin, Heidelberg, New York, 1982.

[92] J. Callaway, Quantum Theory of the Solid State, second ed., Academic Press, New York, 1991.

[93] P. Güttinger, Das Verhalten von Atomen im magnetischen Drehfeld, Zeitschrift Phys. 73 (3) (1932) 169–184, http://dx.doi.org/10.1007/BF01351211.

[94] Clusius, Einführung in die Quantenchemie. Von H. Hellmann. 350 S.,43 Abb., 35 Tab. Franz Deuticke, Leipzig u. Wien 1937. Pr. geh. RM. 20,-. geb. RM. 22, Angew. Chem. 54 (1941) 156.

[95] R.P. Feynman, Forces in molecules, Phys. Rev. 56 (1939) 340–343, http://dx.doi.org/10.1103/PhysRev.56.340, URL https://link.aps.org/doi/10.1103/PhysRev.56.340.

[96] M. Di Ventra, S.T. Pantelides, Hellmann-Feynman theorem and the definition of forces in quantum time-dependent and transport problems, Phys. Rev. B 61 (23) (2000) 16207.

[97] A. Togo, I. Tanaka, First principles phonon calculations in materials science, Scr. Mater. 108 (2015) 1–5, http://dx.doi.org/10.1016/j.scriptamat.2015.07.021, URL https://www.sciencedirect.com/science/article/pii/S1359646215003127.

[98] J. Yang, J. Long, L. Yang, D. Li, First-principles investigations of the physical properties of binary uranium silicide alloys, J. Nucl. Mater. 443 (1) (2013) 195–199, http://dx.doi.org/10.1016/j.jnucmat.2013.07.022, URL https://www.sciencedirect.com/science/article/pii/S0022311513009100.
[99] M. Islam, A comparative investigation on the fundamental physical properties of UX_2 (X=O, N, C, Si and S) solid nuclear fuel materials: A DFT + U study, Chem. Phys. Impact 7 (2023) 100310, http://dx.doi.org/10.1016/j.chphi.2023.100310, URL https://www.sciencedirect.com/science/article/pii/S2667022423001494.
[100] J.-W. Yang, L. An, Lattice vibrational behavior and thermodynamic properties of uranium disilicide USi_2, Solid State Commun. 248 (2016) 47–52, http://dx.doi.org/10.1016/j.ssc.2016.09.010, URL https://www.sciencedirect.com/science/article/pii/S0038109816302502.
[101] Y. Guo, C. Wang, W. Qiu, X. Ke, P. Huai, C. Cheng, Z. Zhu, C. Chen, Structural and electronic phase transitions of ThS_2 from first-principles calculations, Phys. Rev. B 94 (2016) 134104, http://dx.doi.org/10.1103/PhysRevB.94.134104, URL https://link.aps.org/doi/10.1103/PhysRevB.94.134104.
[102] M. Naher, S. Naqib, An ab-initio study on structural, elastic, electronic, bonding, thermal, and optical properties of topological Weyl semimetal TaX (X=P, As), Sci. Rep. 11 (1) (2021) 1–21.
[103] O. Beckstein, J.E. Klepeis, G.L.W. Hart, O. Pankratov, First-principles elastic constants and electronic structure of $\alpha - Pt_2Si$ and PtSi, Phys. Rev. B 63 (2001) 134112, http://dx.doi.org/10.1103/PhysRevB.63.134112, URL https://link.aps.org/doi/10.1103/PhysRevB.63.134112.
[104] Z.-j. Wu, E.-j. Zhao, H.-p. Xiang, X.-f. Hao, X.-j. Liu, J. Meng, Crystal structures and elastic properties of superhard IrN_2 and IrN_3 from first principles, Phys. Rev. B 76 (2007) 054115, http://dx.doi.org/10.1103/PhysRevB.76.054115, URL https://link.aps.org/doi/10.1103/PhysRevB.76.054115.
[105] B. Xiao, J. Feng, C.T. Zhou, Y.H. Jiang, R. Zhou, Mechanical properties and chemical bonding characteristics of Cr_7C_3 type multicomponent carbides, J. Appl. Phys. 109 (2) (2011) 023507, http://dx.doi.org/10.1063/1.3532038.
[106] L. Kleinman, Deformation potentials in silicon. I. Uniaxial strain, Phys. Rev. J. Arch. 128 (1962) 2614–2621, http://dx.doi.org/10.1103/PhysRev.128.2614, URL https://link.aps.org/doi/10.1103/PhysRev.128.2614.
[107] S.-C. Wu, G.H. Fecher, S. Shahab Naghavi, C. Felser, Elastic properties and stability of Heusler compounds: Cubic Co_2YZ compounds with L21 structure, J. Appl. Phys. 125 (8) (2019) 082523, http://dx.doi.org/10.1063/1.5054398.
[108] S. Pugh, XCII. Relations between the elastic moduli and the plastic properties of polycrystalline pure metals, Lond. Edinb. Dubl. Philos. Mag. J. Sci. 45 (367) (1954) 823–843, http://dx.doi.org/10.1080/14786440808520496.
[109] S. Kumar, J. Jung, Mechanical and electronic properties of Ag_3Sn intermetallic compound in lead free solders using ab initio atomistic calculation, Mater. Sci. Eng. B 178 (1) (2013) 10–21, http://dx.doi.org/10.1016/j.mseb.2012.10.003, URL https://www.sciencedirect.com/science/article/pii/S0921510712004849.
[110] X. Zeng, R. Peng, Y. Yu, Z. Hu, Y. Wen, L. Song, Pressure effect on elastic constants and related properties of Ti_3Al intermetallic compound: A first-principles study, Materials 11 (10) (2018) http://dx.doi.org/10.3390/ma11102015, URL https://www.mdpi.com/1996-1944/11/10/2015.
[111] W. Voigt, A determination of the elastic constants for beta-quartz lehrbuch de kristallphysik, Terubner Leipzig 40 (1928) 2856–2860.
[112] A. Reuss, Calculation of the flow limits of mixed crystals on the basis of the plasticity of monocrystals, Z. Angew. Math. Mech. 9 (1929) 49–58.
[113] R. Hill, The elastic behaviour of a crystalline aggregate, Proc. Phys. Soc. Sect. A 65 (5) (1952) 349–354, http://dx.doi.org/10.1088/0370-1298/65/5/307.
[114] J. Lin, L. Wang, Z. Hu, X. Li, H. Yan, First-principles study of Al_2Sm intermetallic compound on structural, mechanical properties and electronic structure, Solid State Commun. 251 (2017) 98–103, http://dx.doi.org/10.1016/j.ssc.2016.12.018, URL https://www.sciencedirect.com/science/article/pii/S003810981630357X.
[115] X. Tao, J. Yang, L. Xi, Y. Ouyang, First-principles investigation of the thermophysical properties of Ca_3Si_4, J. Solid State Chem. 194 (2012) 179–187, http://dx.doi.org/10.1016/j.jssc.2012.05.009, URL https://www.sciencedirect.com/science/article/pii/S0022459612003222.
[116] P. Mao, B. Yu, Z. Liu, F. Wang, Y. Ju, First-principles investigation on mechanical, electronic, and thermodynamic properties of Mg_2Sr under high pressure, J. Appl. Phys. 117 (11) (2015) 115903, http://dx.doi.org/10.1063/1.4915339.
[117] A. Yildirim, H. Koc, E. Deligoz, First-principles study of the structural, elastic, electronic, optical, and vibrational properties of intermetallic Pd_2Ga, Chin. Phys. B 21 (3) (2012) 037101, http://dx.doi.org/10.1088/1674-1056/21/3/037101.
[118] M. Atikur Rahman, M. Hasan, J.F. Lubna, R. Khatun, S. Sarker, M.Z. Hasan, A. Hossain, M.M. Hossain, M. Rasheduzzaman, W. Hasan, N. Jamila, Comparative study of the structural, mechanical, electronic, optical and thermodynamic properties of superconducting disilicide YT_2Si_2 (T=Co, Ni, Ru, Rh, Pd, Ir) by DFT simulation, J. Phys. Chem. Solids 178 (2023) 111342, http://dx.doi.org/10.1016/j.jpcs.2023.111342, URL https://www.sciencedirect.com/science/article/pii/S0022369723001324.
[119] M.A. Rahman, R. Khatun, R. Ferdous, D. Chandra Roy, M.Z. Hasan, A. Irfan, M.A. Razzaque Sarker, M.M. Hossain, A. Hossain, S.C. Mouna, S. Sarker, First-principles calculations to investigate structural, elastic, electronic, optical and thermal properties of La-based ternary intermetallic superconductors LaM_2Si_2 (M=Co, Cu, Rh, Pd, Ag, Ir, Pt, Au), J. Mater. Res. Technol. 26 (2023) 3840–3862, http://dx.doi.org/10.1016/j.jmrt.2023.08.177, URL https://www.sciencedirect.com/science/article/pii/S2238785423019841.
[120] X.-Q. Chen, H. Niu, D. Li, Y. Li, Modeling hardness of polycrystalline materials and bulk metallic glasses, Intermetallics 19 (9) (2011) 1275–1281, http://dx.doi.org/10.1016/j.intermet.2011.03.026, URL https://www.sciencedirect.com/science/article/pii/S0966979511000987.
[121] M.W. Barsoum, M. Radovic, Elastic and mechanical properties of the MAX phases, Annu. Rev. Mater. Res. 41 (1) (2011) 195–227, http://dx.doi.org/10.1146/annurev-matsci-062910-100448.
[122] G.N. Greaves, A.L. Greer, R.S. Lakes, T. Rouxel, Poisson's ratio and modern materials, Nat. Mater. 10 (11) (2011) 823–837.
[123] I. Frantsevich, Elastic Constants and Elastic Moduli of Metals and Insulators, Naukova dumka, 1982, Reference book.
[124] A. Šimůnek, How to estimate hardness of crystals on a pocket calculator, Phys. Rev. B 75 (2007) 172108, http://dx.doi.org/10.1103/PhysRevB.75.172108, URL https://link.aps.org/doi/10.1103/PhysRevB.75.172108.
[125] P. Mott, J. Dorgan, C. Roland, The bulk modulus and Poisson's ratio of "incompressible" materials, J. Sound Vib. 312 (4) (2008) 572–575, http://dx.doi.org/10.1016/j.jsv.2008.01.026, URL https://www.sciencedirect.com/science/article/pii/S0022460X08000771.
[126] H. Fu, D. Li, F. Peng, T. Gao, X. Cheng, Ab initio calculations of elastic constants and thermodynamic properties of NiAl under high pressures, Comput. Mater. Sci. 44 (2) (2008) 774–778, http://dx.doi.org/10.1016/j.commatsci.2008.05.026, URL https://www.sciencedirect.com/science/article/pii/S0927025608002619.
[127] E. Schreiber, O.L. Anderson, N. Soga, et al., Elastic Constants and their Measurement, Vol. 6, McGraw-Hill, New York, 1973.
[128] J. Feng, B. Xiao, R. Zhou, W. Pan, D.R. Clarke, Anisotropic elastic and thermal properties of the double perovskite slab–rock salt layer $Ln_2SrAl_2O_7$ (Ln=La, Nd, Sm, Eu, Gd or Dy) natural superlattice structure, Acta Mater. 60 (8) (2012) 3380–3392, http://dx.doi.org/10.1016/j.actamat.2012.03.004, URL https://www.sciencedirect.com/science/article/pii/S1359645412001772.
[129] J. Yang, M. Shahid, C. Wan, F. Jing, W. Pan, Anisotropy in elasticity, sound velocities and minimum thermal conductivity of zirconia from first-principles calculations, J. Eur. Ceram. Soc. 37 (2) (2017) 689–695, http://dx.doi.org/10.1016/j.jeurceramsoc.2016.08.034, URL https://www.sciencedirect.com/science/article/pii/S0955221916304708.
[130] W.L. McMillan, Transition temperature of strong-coupled superconductors, Phys. Rev. J. Arch. 167 (1968) 331–344, http://dx.doi.org/10.1103/PhysRev.167.331, URL https://link.aps.org/doi/10.1103/PhysRev.167.331.
[131] M. Fine, L. Brown, H. Marcus, Elastic constants versus melting temperature in metals, Scr. Metall. 18 (9) (1984) 951–956, http://dx.doi.org/10.1016/0036-9748(84)90267-9, URL https://www.sciencedirect.com/science/article/pii/0036974884902679.
[132] M.F. Ashby, P.J. Ferreira, D.L. Schodek, Chapter 4 - Material classes, structure, and properties, in: M.F. Ashby, P.J. Ferreira, D.L. Schodek (Eds.), Nanomaterials, Nanotechnologies and Design, Butterworth-Heinemann, Boston, 2009, pp. 87–146, http://dx.doi.org/10.1016/B978-0-7506-8149-0.00006-4, URL https://www.sciencedirect.com/science/article/pii/B9780750681490000064.
[133] D.R. Clarke, Materials selection guidelines for low thermal conductivity thermal barrier coatings, Surf. Coat. Technol. 163–164 (2003) 67–74, http://dx.doi.org/10.1016/S0257-8972(02)00593-5, URL https://www.sciencedirect.com/science/article/pii/S0257897202005935. Proceedings of the 29th International conference on Metallurgical Coatings and Thin Films.
[134] D.G. Cahill, S.K. Watson, R.O. Pohl, Lower limit to the thermal conductivity of disordered crystals, Phys. Rev. B 46 (1992) 6131–6140, http://dx.doi.org/10.1103/PhysRevB.46.6131, URL https://link.aps.org/doi/10.1103/PhysRevB.46.6131.
[135] V. Tvergaard, J.W. Hutchinson, Microcracking in ceramics induced by thermal expansion or elastic anisotropy, J. Am. Ceram. Soc. 71 (3) (1988) 157–166, http://dx.doi.org/10.1111/j.1151-2916.1988.tb05022.x, URL https://ceramics.onlinelibrary.wiley.com/doi/abs/10.1111/j.1151-2916.1988.tb05022.x.
[136] S.I. Ranganathan, M. Ostoja-Starzewski, Universal elastic anisotropy index, Phys. Rev. Lett. 101 (2008) 055504, http://dx.doi.org/10.1103/PhysRevLett.101.055504, URL https://link.aps.org/doi/10.1103/PhysRevLett.101.055504.
[137] D.H. Chung, W.R. Buessem, The elastic anisotropy of crystals, J. Appl. Phys. 38 (5) (1967) 2010–2012, http://dx.doi.org/10.1063/1.1709819.
[138] X. Gao, Y. Jiang, R. Zhou, J. Feng, Stability and elastic properties of Y–C binary compounds investigated by first principles calculations, J. Alloys Compd. 587 (2014) 819–826, http://dx.doi.org/10.1016/j.jallcom.2013.11.005, URL https://www.sciencedirect.com/science/article/pii/S0925838813027357.
[139] S. Mitro, M. Hadi, F. Parvin, R. Majumder, S. Naqib, A. Islama, Effect of boron incorporation into the carbon-site in Nb_2SC MAX phase: Insights from DFT, J. Mater. Res. Technol. 11 (2021) 1969–1981, http://dx.doi.org/10.1016/j.jmrt.2021.02.031, URL https://www.sciencedirect.com/science/article/pii/S2238785421001563.
[140] V. Milman, M.C. Warren, Elasticity of hexagonal BeO, J. Phys.: Condens. Matter 13 (2) (2000) 241–251, http://dx.doi.org/10.1088/0953-8984/13/2/302.
[141] A. Marmier, Z.A. Lethbridge, R.I. Walton, C.W. Smith, S.C. Parker, K.E. Evans, ElAM: A computer program for the analysis and representation of anisotropic elastic properties, Comput. Phys. Comm. 181 (12) (2010) 2102–2115, http://dx.doi.org/10.1016/j.cpc.2010.08.033, URL https://www.sciencedirect.com/science/article/pii/S0010465510003401.